E4F1 COORDINATES PYRUVATE METABOLISM AND THE ACTIVITY OF THE ELONGATOR COMPLEX TO ENSURE PROTEIN TRANSLATION FIDELITY DURING NEURONAL DEVELOPMENT

Di Michele Michela[1*], Attina Aurore[2], Laguesse Sophie[3], De Blasio Carlo[1], Wendling Olivia[4], Frenois Francois-Xavier[5], Encislai Betty[1], Fuentes Maryse[1], Jahanault-Tagliani Céline[1], Rousseau Mélanie[1], Roux Pierre-François[1], Guégan Justine[6], Buscail Yoan[1,7], Dupré Pierrick[1], Michaud Henri-Alexandre[8], Rodier Geneviève[1], Bellvert Floriant[9], Kulyk Barbier Hannah[9], Ferraro Peyret Carole[10,11], Mathieu Hugo[1], Chaveroux Cédric[10], Pirot Nelly[1,7], Rubio Lucie[1], Torro Adeline[1], Compan Vincent[12], Sorg Tania[4], Ango Fabrice[13], David Alexandre[2,12], Lebigot Elise[14], Legati Andrea[15], Hirtz Christophe[3], Ghezzi Daniele[15,16], Nguyen Laurent[3], Sardet Claude[1], Lacroix Matthieu[1,17*] and Le Cam Laurent[1,17*].

[1] *Institut de Recherche en Cancérologie de Montpellier (IRCM), INSERM U1194; Univ. Montpellier, Institut régional du Cancer de Montpellier (ICM), Montpellier, F-34298, France.*

[2] *IRMB-PPC, Univ Montpellier, INSERM, CHU Montpellier, CNRS, Montpellier, France.*

[3] *GIGA-Stem Cells, Interdisciplinary Cluster for Applied Genoproteomics (GIGA-R), University of Liège, C.H.U. Sart Tilman, Liège 4000, Belgium.*

[4] *Université de Strasbourg, CNRS, INSERM, CELPHEDIA, PHENOMIN, Institut Clinique de la Souris (ICS), 1 rue Laurent Fries, 67404 Illkirch, France.*

[5] *Department of Pathology, CHU, Imag'IN Platform, IUCT-Oncopole, Toulouse, 31059, France.*

[6] *Data Analysis Core Platform, Institut du Cerveau – Paris Brain Institute - ICM, Sorbonne Université, INSERM, CNRS, APHP, Hôpital de la Pitié-Salpêtrière, 75013 Paris, France.*

[7] *BioCampus, RHEM, Université de Montpellier, CNRS, INSERM, Montpellier, France.*

[8] *Mass cytometry imaging plateform, Institut de Recherche en Cancérologie de Montpellier (IRCM), Institut régional du Cancer de Montpellier (ICM), Montpellier, F-34298, France.*

[9] *MetaToul- MetaboHUB, National Infrastructure of Metabolomics and Fluxomics, Toulouse F-31077, France.*

[10] *Univ Lyon, Claude Bernard University, Cancer Research Center of Lyon, INSERM 1052, CNRS5286, Faculty of Pharmacy, F-69008, Lyon, France.*

[11] *Hospices Civils de Lyon, AURAGEN, Edouard Herriot Hospital, F-69003, Lyon, France.*

[12] *IGF, Univ. Montpellier, CNRS, INSERM, Montpellier, France.*

[13] *INM, Univ Montpellier, INSERM, CNRS, Montpellier France.*

[14] *Biochemistry Department, Bicêtre Hospital, APHP Paris Saclay, Le Kremlin Bicêtre, France.*

[15] *Unit of Medical Genetics and Neurogenetics, Fondazione IRCCS Istituto Neurologico CarloBesta, 20126 Milan, Italy.*

[16] *Department of Pathophysiology and Transplantation (DEPT), University of Milan, 20122, Milan, Italy.*

[17] *co-senior authors.*

[*] *Corresponding authors: michela.dimichele@inserm.fr (MDM), matthieu.lacroix@inserm.fr (LM), laurent.lecam@inserm.fr (LCL).*

Keywords: E4F1, Leigh syndrome, pyruvate metabolism, Elongator, translation, integrated stress response

Running title: E4F1 regulates translation fidelity through the Elongator complex in neurons

SUMMARY

The Leigh syndrome is a severe inborn neurodegenerative encephalopathy commonly associated with pyruvate metabolism defects. The transcription factor E4F1, a key regulator of the pyruvate dehydrogenase (PDH) complex (PDC), was previously found to be mutated in Leigh syndrome patients, but the molecular mechanisms leading to cell death in E4F1-deficient neurons remain unknown. Here, we show that E4F1 directly regulates *Dlat* and *Elp3*, two genes encoding key subunits of the PDC and of the Elongator complex, to coordinate AcetylCoenzyme A production and its utilization to acetylate tRNAs. Genetic inactivation of *E4f1* in neurons during mouse embryonic development impaired tRNAs editing and induced an ATF4-mediated integrated stress response (ISR), leading to neuronal cell death and microcephaly. Furthermore, our analysis of PDH-deficient cells unraveled a crosstalk linking the PDC to ELP3 expression that is perturbed in Leigh syndrome patients. Altogether, our data support a model where pyruvate metabolism regulates the epitranscriptome to ensure protein translation fidelity.

INTRODUCTION:

The Leigh syndrome (OMIM#256000) is a severe neurodegenerative disease affecting one in forty thousand newborns that stems from mitochondrial deficiencies in pyruvate metabolism or in the electron transport chain (ETC). Mutations in over seventy-five genes have been linked to this inborn metabolic disorder, including mutations in genes encoding key components or regulators of the pyruvate dehydrogenase (PDH) complex (PDC), a mitochondrial multisubunit complex that converts pyruvate into AcetylCoenzymeA (AcCoA) to fuel the tri-carboxylic acid cycle (TCA). Leigh syndrome patients display chronic lactate acidemia and bilateral necrotizing lesions of the basal ganglia and the brain stem. Affected children develop a broad range of motor and neurological symptoms, including muscular atonia, growth and mental retardation, ataxia and vision loss. No efficient cure has been identified so far for this life-threatening disease which results in early death although few patients have shown a partial improvement of their clinical symptoms under a ketogenic diet, a regimen that metabolically bypasses the PDC complex, or upon its pharmacological stimulation by dichloro-acetate (DCA) (Bakare et al., 2021). Paradoxically, despite most of the genetic alterations implicated in the Leigh syndrome have been identified, the molecular mechanisms underlying the clinical symptoms of these children, and in particular their neurological defects, remain poorly understood.

The multifunctional protein E4F1 was recently linked to the Leigh syndrome. Thus, two siblings harboring a homozygous *E4F1*^{K144Q} missense mutation developed clinical symptoms reminiscent of those observed in Leigh syndrome patients, including muscular hypotonia, microcephaly, hyperlactacidemia and organic aciduria. Brain MRI-imaging revealed symmetric necrotic lesions in the subthalamic nuclei and in the substantia nigra (Legati et al., 2016). The E4F1 protein was originally identified as a transcriptional regulator of the E4 viral gene that is hijacked by the viral oncoprotein E1A during adenoviral infection (Raychaudhuri et al., 1987). Since, E4F1 was also characterized as an atypical E3 ligase of the tumor suppressor p53 that controls its transcriptional activities independently of degradation (Le Cam et al., 2006). Beside its role in regulating the balance between cell proliferation and cell death (Fajas et al., 2001;

2000; Le Cam et al., 2006; Rizos et al., 2003), E4F1 was also identified as a major regulator of the PDC complex. Thus, E4F1 directly binds to the promoter region of several genes encoding essential subunits or regulators of the PDC complex, including DLAT and DLD, the E2 and E3 core subunits of the PDC, the regulatory subunit of the PDH phosphatase complex PDPR, the pyruvate transporter of the inner mitochondrial membrane MPC1, and the SLC25A19 protein involved in mitochondrial uptake of thiamine pyrophosphate, an essential co-factor of the PDC (Goguet-Rubio et al., 2016; Lacroix et al., 2016; Rodier et al., 2015). Consistently, knock-out (KO) mice lacking E4F1 in their skeletal muscles exhibit decreased PDC activity and display phenotypes that are reminiscent of some of the clinical symptoms of Leigh syndrome patients, including chronic lactate acidemia and exercice intolerance (Lacroix et al., 2016). However, no major neurological defects were observed in this animal model, suggesting that the neuronal cell death observed in Leigh syndrome patients results from cell autonomous defects. In this work, we generated mice lacking E4F1 in the central nervous system (CNS) to investigate its role during neuronal development. Detailed molecular characterization of this animal model during embryonic development and of E4F1-deficient primary fibroblasts demonstrated that in addition to its role in pyruvate metabolism, E4F1 is also a key transcriptional regulator of *Elp3*, a gene encoding the catalytic subunit of the Elongator complex. Elongator is an acetyl-transferase which targets a subset of tRNAs in the acceptor stem loop at the wobble position uridine 34 (U_{34}) to promote a stepwise cascade of chemical modifications (thiolation and methoxy-carbonyl-methylation) to produce mature tRNAs to ensure protein translation fidelity (Abbassi et al., 2020; Hermand, 2020; Lin et al., 2019). Perturbation of E4F1-mediated control of the Elongator complex during embryonic development resulted in severe brain defects and microcephaly that are associated with the impairment of tRNA editing and the induction of an integrated stress / unfolded protein response (ISR/UPR) and neuronal cell death. Moreover, we identified a previously unknown crosstalk between the PDC and ELP3 expression that is perturbed in cells isolated from Leigh syndrome patients. Altogether, our data highlight the importance of the links between pyruvate metabolism and tRNAs editing to ensure proteome homeostasis in the CNS.

RESULTS:

E4F1 plays a critical role in neuronal development.

To evaluate the roles of *E4f1* during neuronal development, we generated animals lacking E4F1 in their CNS by crossing *E4f1* constitutive and conditional Knock-out (KO) mice with transgenic animals expressing the CRE recombinase under the control of the *Nestin* promoter that is predominantly active in all neural progenitors, and with a reporter strain allowing Cre-mediated expression of the green fluorescent protein (GFP) from the ROSA26 locus (Supplemental Fig. S1A) (Lacroix et al., 2010; Le Cam et al., 2004; Muzumdar et al., 2007; Tronche et al., 1999). In these compound mutant animals (hereafter referred to as *E4f1*$^{(Nes)KO}$) and their control littermates (CTL), immunohistochemistry (IHC) analysis of the GFP reporter on head or whole embryo sagittal sections isolated at different developmental stages confirmed that Cre-mediated recombination was mainly restricted to the CNS and the spinal cord (Fig. 1A and Supplemental Fig. S1B). The efficiency and the specificity of Cre-mediated inactivation of *E4f1* in the CNS was confirmed at E14.5 by immunoblotting and RT-qPCR, respectively (Fig. 1B,C). *E4f1*$^{(Nes)KO}$ mice were represented at the expected mendelian ratio at E14.5, E16.5 and E18.5 and showed no obvious growth developmental abnormalities, but were absent at P1, indicating that E4F1 deficiency in the CNS leads to perinatal death (Fig. 1D and Supplemental Fig. S1C,D). Moreover, *E4f1*$^{(Nes)KO}$ E18.5 embryos exhibited a microcephaly that is comparable to that observed in Leigh syndrome patients (Supplemental Fig. S1E).

Next, we performed high-resolution episcopic microscopy (HREM) and generated three-dimension (3D) volumic brain reconstructions of E14.5 and E16.5 *E4f1*$^{(Nes)KO}$ embryos and CTL littermates to evaluate the morphology of different regions of the CNS (Fig. 1E,F and Supplemental Fig. S2A,B). These analyses revealed that the forebrain, midbrain and hindbrain neuroepithelium of E16.5 *E4f1*$^{(Nes)KO}$ embryos presented large areas of degeneration. These defects were illustrated by patchy losses of neuroepithelium or as areas of ballooning leading to alterations in the structure of all regions of the brain. The space between the brain and the cranium was also enlarged in E4F1-deficient mutants when compared to control littermates.

3D reconstructions showed that the volume of the total and subdivided neural tissues (forebrain, midbrain, hindbrain) was smaller in *E4f1*$^{(Nes)KO}$ E16.5 embryos, whereas the volume of the total and subdivided ventricles was bigger in E4F1-deficient animals than in control littermates. Minor brain lesions were detected in the forebrain, but not in the midbrain and hindbrain, at E14.5, suggesting that the brain defects resulting from E4F1 deficiency started at E14.5 and worsened at later stages of embryonic development (Fig. 1E-F and supplemental Fig. S2A,B). Histological analyses of hematoxylin and eosin (H&E)-stained sagittal sections of E14.5, E16.5 and E18.5 embryos confirmed the structural lesions observed by HREM and showed that these brain defects started at E14.5 and increased at later developmental stages. The thickness of the cortical plate (CP), which is enriched in neurons, was reduced in E14.5 *E4f1*$^{(Nes)KO}$ embryos. E4F1 deficiency in CNS resulted in decreased cellularity of all cortical layers (Supplemental Fig. S2C). Moreover, IHC and immunoblot analyses showed increased cleavage of the apoptotic marker caspase 3 (C-Casp3) at E16.5 and E18.5, but not at E14.5 (Fig. 2A-C). To identify the neural populations in which E4F1 plays an important role, we determined in coronal brain sections prepared from E14.5 embryos the number of apical and intermediate progenitors, as well as that of neurons, identified on the basis of SOX2, TBR2 and TBR1 expression, respectively (Supplemental Fig. S2D,E). The number of TBR2 positive intermediate progenitors, and that of TBR1 neurons decreased in the brain of *E4f1*$^{(Nes)KO}$ E14.5 embryos, whereas the number of SOX2 positive apical progenitors remained comparable to that of control animals. We also evaluated the expression of C-Casp3 and of the proliferation marker Ki67 (Fig. 2D). These *in situ* analyses showed that E4F1 deficiency impaired the proportion of cycling progenitors, likely explaining the decreased cellularity observed in various regions of the neuroepithelium. Moreover, and consistently with our previous findings, no C-Casp3 staining was observed at E14.5, suggesting that the proliferation defects of E4F1-deficient progenitors at E14.5 preceded neuronal cell death at later stages of development. Altogether, these data indicate that E4F1 plays a critical role in neuronal proliferation and cell survival during mid-corticogenesis and that perturbation of E4F1 neuronal functions results in microcephaly and perinatal death.

Identification of E4F1-controlled transcriptional program in neurons.

To gain insights into the molecular mechanisms underlying impaired neurogenesis in E4F1-deficient neurons, we compared the gene expression profile of total brains harvested from *E4f1*$^{(Nes)KO}$ and CTL embryos at E14.5 using RNA sequencing (RNA-seq). Upon *E4f1* inactivation in the CNS, 185 genes displayed a fold change superior to 2 with a false discovery rate (FDR) inferior to 0.05, among which 116 were significantly down-regulated and 69 were up-regulated. Among the top 35 differentially expressed transcripts with the lowest false discovery rate (FDR, adjusted p value) in E4F1-deficient neurons were *Wdr7*, *Kif1bp*, *Neurl4*, *Fktn*, *Dlat*, *Znhit6*, *Senp8*, *Tube1*, *Elp3*, *Leo1*, *Tti2*, *Dph5*, *Taz*, *Prbm1, Ddi2*, *Mrfap1*, *Taz, Dnajc19*, *Mrpl15*, *Nsun5* and *Rad52* (Fig. 3A,B, supplemental Fig. S3A and supplemental table 1). Interestingly, these genes were previously identified as E4F1-direct target genes in mouse fibroblasts and ES cells by chromatin immunoprecipitation (ChIP) combined with deep sequencing (ChIP-seq) (Lacroix et al., 2016; Rodier et al., 2015). Gene set enrichment analysis (GSEA) indicated that this E4F1-signature was significantly down-regulated in E4F1-deficient neurons, highlighting an E4F1 core transcriptional program that is regulated in multiple cell types (Fig. 3C, supplemental Fig. S3B and supplemental table 2). Impaired expression of a subset of genes composing this core E4F1 program was confirmed by RT-qPCR on mRNAs extracted from total brains or forebrains of E14.5 *E4f1*$^{(Nes)KO}$ embryos (Fig. 3D and supplementary Fig. S3C). Of note, GSEA analysis also indicated that in addition to the deregulation of this E4F1 core program, an ISR/UPR was clearly induced in E4F1-deficient neurons (Fig. 3E-F and supplemental Fig. S3D).

E4F1 regulates the PDC complex and pyruvate metabolism in the CNS

Among the top three most deregulated genes identified by RNA-seq in the brain of *E4f1*$^{(Nes)KO}$ embryos was *Dlat*, an E4F1-direct target gene encoding the E2 subunit of the PDC complex. Interestingly, RT-qPCR analysis of mRNAs prepared from E14.5 *E4f1*$^{(Nes)KO}$ forebrains indicated that the role of E4F1 in the regulation of the PDC in neurons extended to

other E4F1-direct target genes encoding several key subunits or regulators of the PDC, including *Dld*, *Mpc1*, *Slc25a19*, and *Pdpr* (Fig. 4A). Furthermore, immunoblot analyses confirmed that *E4f1* inactivation in neurons impinged on DLAT and MPC1 protein levels, whereas those of PDHA1, the E1 subunit of the PDC complex, that were evaluated as a control, and DLD, remained unaffected (Fig. 4B). Consistent with this expression profile, PDH activity was strongly impaired in the brain of *E4f1*$^{(Nes)KO}$ embryos and resulted in increased blood lactate levels (Fig. 4C,D). Moreover, IHC analyses indicated that the protein levels of the lactate transporter MCT4 were upregulated in the brain of E4F1-deficient embryos (Fig. 4E). Altogether, these data show that *E4f1* inactivation in neurons impacts on pyruvate oxidation by the PDC and favors the redirection of the glycolytic flux towards lactate production, a feature reminiscent of the metabolic reprogramming occurring in Leigh syndrome patients.

E4f1 **controls the Elongator complex in neurons**

Strikingly, our RNA-seq datasets indicated that *Elp3* mRNA levels were also strongly reduced in E4F1-deficient brains (Fig. 3A,B). *Elp3* encodes the catalytic subunit of the Elongator complex, an acetyl-transferase that was previously implicated in neurogenesis (Laguesse et al., 2015). This prompted us to further investigate the links between E4F1 and the Elongator complex. Analysis of previous ChIP-seq experiments performed in murine embryonic fibroblasts (Mefs) and ES cells suggested that *Elp3* is a direct target gene of E4F1 (Fig. 5A) (Houlès et al., 2015; Rodier et al., 2015). Quantitative ChIP (qChIP) experiments performed with a validated polyclonal anti-E4F1 antibody confirmed that E4F1 binds to the promoter region of *Elp3* on its canonical binding site in neuronal N2A cells (Fig. 5B). We then determined by RT-qPCR the mRNA levels of different key subunits of the Elongator complex in the brain of *E4f1*$^{(Nes)KO}$ embryos. Consistent with the role of E4F1 in the direct regulation of *Elp3* transcription, *Elp3* mRNA levels were reduced in E14.5 E4F1-deficient brains, whereas those of *Elp1*, *Elp2* and *Elp4*, remained unchanged (Fig. 5C). At later developmental stages (E16.5 and E18.5), the mRNA levels of all these core subunits of the Elongator complex were affected by E4F1 deficiency (Supplemental Fig. S4A). Immunoblots showed that *E4f1*

inactivation also impacted on ELP3 protein levels (Fig. 5D). In line with previous reports showing that the stability of the catalytic subunit ELP3 and that of the scaffold ELP1 are interdependent (Laguesse et al., 2015; Petrakis et al., 2004), ELP1 protein levels also decreased in the brain of E14.5 *E4f1*$^{(Nes)KO}$ embryos (Fig. 5D).

Next, we explored the impact of E4F1-deficiency on the activity of the Elongator complex. The Elongator complex promotes the modifications of a subset of tRNAs (tRNAs-Gln, tRNAs-Glu and tRNA-Lys) modifications by acetylating the uridine located at position 34 of the anti-codon stem loop (U_{34}). This acetylation reaction initiates a stepwise cascade that first leads to the attachment of a carboxy-methyl group (cm^5U_{34}) which is further processed by other enzymes (including Trm9, Trm112 and a thiolase) to generate 5-carbamoylmethyl uridine (ncm^5U_{34}), 5-methoxycarbonylmethyl uridine (mcm^5U_{34}) and its thiolated isoform 5-methoxy-carbonyl-methyl-2-thio uridine ($mcm^5s^2U_{34}$) (Supplemental Fig. S4B)(Abbassi et al., 2020; Hermand, 2020). Liquid-chromatography coupled to tandem Mass Spectrometry (LC-MS/MS) analysis of tRNAs purified from E14.5 *E4f1*$^{(Nes)KO}$ and CTL brains showed that the relative abundance of ncm^5U_{34} and $mcm^5s^2U_{34}$ decreased in E4F1-deficient neurons, whereas that of other tRNAs modifications not linked to the Elongator complex, including 3-methylcytosine (m3C) and methylguanosine (Gm), remained unchanged (Fig. 5E). RT-qPCR analyses showed that the total amount of tRNAs targeted by the Elongator complex, tRNAs-Gln, tRNAs-Glu and tRNA-Lys, were comparable in the brain of E14.5 *E4f1*$^{(Nes)KO}$ and CTL embryos, demonstrating that the decreased abundance of $mcm^5s^2U_{34}$ and ncm^5U_{34} in E4F1-deficient neurons was not the consequence of impaired production of these tRNAs (Supplemental Fig. S4C). Since the Elongator complex has also been involved in tubulin and histone acetylation, we evaluated the ratio of acetylated/total tubulin (α-TUBac/TUB) and that of acetylated histone H3 on lysine 14/total Histone H3 (H3K14ac/H3) (Creppe et al., 2009; Winkler et al., 2002). We failed to detect any significant difference in α-TUBac nor in H3K14ac, indicating that E4F1 deficiency in neurons, and the associated impaired Elongator complex activity, only impinged on tRNAs editing (Supplemental Fig. S4D).

Previous findings showed that genetic inactivation of *Elp3* during corticogenesis leads to the induction of an UPR mediated by members of the Activating Transcription Factor (ATF) family (Laguesse et al., 2015). Consistent with these findings, IHC analysis of brain sections prepared from E14.5 *E4f1*$^{(Nes)KO}$ embryos confirmed the induction of ATF4 protein levels in E4F1-deficient neurons (Fig. 5F). Furthermore, the induction of this ATF4-driven transcriptional response correlated with activation of its upstream regulator EiF2a, as evidenced by its increased phosphorylation (Fig. 5G). In agreement with these data, RNA-seq and RT-qPCR analyses indicated that E4F1 deficiency in neurons led to increased mRNA levels of ATF4-target genes implicated in the ISR/UPR, including *Atf3*, *Atf5*, *Eif4ebp1, Asns*, *Sesn2*, *Slc6a9*, *Chop*, *Chac1*, *Trib3*, *Mthfd2*, *Slc3a2* and *Slc7a5* (Figs. 3, 5H and supplemental table S1). The ISR involves the derepression of integral ER membrane proteins that activate independent signaling pathways (Hetz et al., 2020). Similarly to the situation in *Elp3* KO neurons, the mRNA levels of *Xbp1* and its spliced transcripts *Xbp1-u* and *Xbp1-s*, as well as those of *Atf6*, remained unchanged in E4F1-deficient neurons, suggesting that *E4f1* inactivation specifically activated the branch of the ISR implicating the PERK kinase and ATF4, but not those implicating IRE1a or ATF6 (Fig. 5H). Altogether, our data support a model in which perturbation of E4F1-mediated control of the Elongator complex impacts on proteome homeostasis leading to the induction of an ISR/UPR and ultimately to neuronal cell death.

E4F1 coordinates pyruvate-derived AcCoA production by the PDC and tRNA editing

The key role of E4F1 in pyruvate metabolism and in the regulation of the Elongator complex prompted us to evaluate whether E4F1 coordinates, at the transcriptional level, the production of pyruvate-derived AcCoA by the PDC and its utilization by the Elongator complex to promote tRNAs editing and ensure protein translation fidelity. To challenge this hypothesis, we first evaluated *Dlat* and *Elp3* expression upon acute *E4f1* inactivation in Mefs. E4F1-deficient Mefs exhibited impaired *Dlat* and *Elp3* mRNA and protein levels (Fig. 6A,B). Moreover, and consistent with our findings in *E4f1*$^{(Nes)KO}$ embryos, these cells also exhibited decreased amounts of $mcm^5s^2U_{34}$ and ncm^5U_{34} (Fig. 6C). Next, we performed stable isotope

tracing experiments to evaluate whether pyruvate-derived AcCoA produced by the PDC serves as a co-factor and a carbon source for the Elongator complex to acetylate tRNAs at U_{34}. Mefs were incubated in presence of uniformally labelled ^{13}C-pyruvate for 6h and we then measured by LC-MS/MS ^{13}C-enrichment in the ionized fragments of ncm^5U_{34} and $mcm^5s^2U_{34}$ that were predicted to include the 2 heavy carbons of the acetyl-group provided by pyruvate-derived ^{13}C-AcCoA into the side chain of the uridine ring upon acetylation by the Elongator complex (Supplementary Fig. S5A). The m+2 isotopologues of ncm^5U_{34} and $mcm^5s^2U_{34}$ were significantly detected in Mefs incubated with ^{13}C-pyruvate for 6h, a process affected upon pre-incubation with UK-5099, a pharmacological inhibitor of the pyruvate mitochondrial transporter MPC1 that indirectly blocks PDH activity (Fig. 6D,E). Hence, these data demonstrate that pyruvate-derived AcCoA produced by the PDC directly contributes to U_{34} tRNAs editing by the Elongator complex.

PDH deficiency impacts on ELP3 expression

To further understand the relationship between pyruvate metabolism and the Elongator complex, we depleted PDHA1 in Mefs using two independent shRNAs. Strikingly, *Pdha1* knock-down (KD) cells displayed decreased ELP3 protein levels, unraveling a previously unknown crosstalk between the PDC and ELP3 expression (Fig. 6F). Consistently, we noticed that skin fibroblasts isolated from Leigh syndrome patients harboring mutations in the *PDHA1* or the *E4F1* genes, but not in those with mutations in *SURF1* or *NDUFS6*, also displayed reduced ELP3 protein levels (Fig. 6G). Since the Leigh syndrome is a monogenic disease, we next evaluated the effect of expressing ectopic wild-type (WT) PDHA1 on endogenous ELP3 protein levels in these patient-derived *PDHA1*-mutated cells. Expression of ectopic flag-tagged WT-PDHA1 increased ELP3 protein levels, confirming that modulating PDC activity impinges on ELP3 expression (Fig. 6H). Altogether, these data support a model where the activities of the PDC and the Elongator complexes are coordinated to ensure tRNAs editing.

DISCUSSION

The Leigh Syndrome is a severe pediatric neurodegenerative disease linked to either PDC or ETC deficiencies. The prognosis for Leigh syndrome patients is very poor and current treatments provide limited improvement of their clinical symptoms. The paucity of animal models recapitulating PDC deficiency has limited studies aiming at understanding the molecular defects underlying the clinical symptoms of Leigh syndrome patients and the development of efficient treatments. Moreover, because the relative contribution of cell autonomous versus systemic metabolic defects to the various clinical manifestations associated with Leigh syndrome remain elusive, the development of genetically engineered mouse models allowing tissue specific inactivation of genes related to the Leigh syndrome is of major interest. To address these questions, we generated a conditional KO mouse strain allowing Cre-mediated inactivation of *E4f1*, a gene mutated in Leigh syndrome encoding a key transcriptional regulator of the PDC. Using this mouse strain, we initially showed that animals lacking E4F1 in skeletal muscles develop normally and do not display any obvious neurological abnormalities, but exhibit muscular endurance defects and chronic lactate acidemia similarly to Leigh syndrome patients (Lacroix et al., 2016). Here, we report the generation and the detailed characterization of a complementary mouse model that we used to genetically inactivate *E4f1* in the CNS during embryonic development and show that these animals develop severe neurological defects leading to microcephaly, one of the common clinical manifestations of Leigh syndrome affected children. We used this animal model to further characterize the molecular defects of E4F1-deficient neurons, and consistent with our previous findings, we confirmed the importance of E4F1 in the regulation of the PDC. Unexpectedly, we also found that E4F1 directly controls at the transcriptional level *Elp3*, a gene encoding the catalytic subunit of the Elongator complex, a multisubunit acetyl-transferase which promotes the production of a subset of mature tRNAs. Finally, our analyses highlighted a previously unknown crosstalk between the PDC and ELP3 that is perturbed in cells isolated from PDH-deficient patients, suggesting that impairement of protein translation fidelity is a common feature of cells exhibiting impaired PDH activity.

How metabolic perturbations lead to changes in gene expression is a field of active research. Many studies highlighted the role of different metabolites, including AcCoA and S-Adenosyl-Methionine (SAM), in the regulation of the epigenome. By serving as essential co-factors of acetyltransferases and methyltransferases, these metabolites directly contribute to DNA or histone modifications, thereby influencing transcription (Morrison, 2022; Nitsch et al., 2021; Sun et al., 2021). Although it is known for decades that some of these acetyl- or methyl-transferases also target RNAs, including mRNAs, tRNAs, or ribosomal RNAs, the importance of their metabolic co-factors in regulating the epitranscriptome remains poorly understood. Previous work showed that serine metabolism in mitochondria provides methyl donors to produce the taurinomethyluridine base at the wobble position of some mitochondrial tRNAs, thereby controlling mitochondrial translation of OXPHOS-related transcripts encoded by the mitochondrial genome (Morscher et al., 2018). In our study, we validated an innovative stable isotope tracing approach to track the metabolic fate of pyruvate-derived carbons into U_{34} tRNAs modifications and demonstrated that AcCoA produced by the PDC directly contributes to tRNAs modifications linked to the Elongator complex. Altogether, our data support a model where E4F1 regulates a transcriptional program coordinating AcCoA production by the PDC and its utilization by the Elongator complex to promote tRNAs editing. Perturbation of this program decreases the abundance of tRNAs modifications initiated by the Elongator complex, and likely as the result of impaired protein translation fidelity, leads to the induction of an ISR and ultimately to neuronal cell death.

It is noteworthy that some antibiotics, including tetracyclines, have been shown recently to improve the fitness of nutrient-deprived cells isolated from patients suffering mitochondrial diseases with deficiencies in the ETC. Strikingly, tetracycline analogues, such as doxycycline, selectively attenuate mitochondrial translation in these cells, and when administrated to *Ndufs4*-mutant animals, improved their neuronal defects and prolonged significantly their lifespan. Although these antibiotics induced a clear ATF4-driven cellular response, their protective effects was rather attributed to the induction of a mitohormetic response which restored a proper redox balance and thereby improved cell survival (Perry et

al., 2021). These results suggest that modulating mitochondrial translation, a process amenable to pharmacological intervention, plays a pivotal role in protecting cells exhibiting ETC deficiency. In the case of E4F1-deficient neurons, it is possible that the ATF4-driven ISR is a protective mechanism induced in response to translation fidelity defects rather than a pathway contributing to neuronal cell death. Interestingly, previous studies also suggested that inhibiting mTORC1 activity, activating a hypoxic response or modulating NAD metabolism, can partly rescue phenotypes associated to respiratory chain deficiencies (Jain et al., 2016; Johnson et al., 2013; Lee et al., 2019). The efficacy of these approaches in case of PDH-deficient-related mitochondrial diseases has not been evaluated yet. Our data pave the way for further studies aiming at evaluating whether the interplay between the PDC and the Elongator complex also represents a new avenue for therapeutic interventions for this devastating disease.

METHODS:

Animal housing

The following strains were used in this study: *E4f1*$^{tm1.1Llca}$, *E4f1*^{tm1Pisc}, *Tg(Nes-cre)*^{1Kln}, *Gt(ROSA)26Sor*$^{tm1(cre/ERT2)Tyj}$ (Le Cam et al., 2004; Lacroix et al., 2010; Tronche et al., 1999, Muzumdar et al., 2007). Mice were interbred and maintained on a mix 129Sv/J; C57Bl/6J background and were housed in a pathogen free barrier facility (room temperature 22 °C; relative humidity 55%, and a 12-h-light–dark cycle). All procedures were approved by the ethic committee for animal warefare of the region Languedoc Roussillon (Comité d'Ethique en Expérimentation Animal Languedoc-Roussillon), an accredited institution of the French Minister for Education, Research and Innovation (agreement number #18030-201812111250227). Animal housing and euthanasia were performed in accordance to the 3R rule. Mice were maintained under chow (A03, Safe) containing 22 kcal% protein, 65 kcal% carbohydrate and 13 kcal% fat. Mice were genotyped by PCR on tail genomic DNA using Red-N extract kit (Sigma), with primers indicated in Supplemental table S3.

Patient material

Skin fibroblasts were isolated from Leigh syndrome patients or control individuals recruited at Paris Kremlin Bicêtre hospital or at the Foundation IRCSS Institute of Neurology Carlo Besta (Milan, Italy), after they signed a written informed consent authorizing their participation in the study and publication of personal clinical information after anonymization.

Cell culture

Mouse embryonic fibroblasts (MEFs) were isolated from E13.5 *E4f1*$^{-/flox}$; *Rosa26-CRE*^{ER} embryos and cultured in DMEM complemented with 10% of heat-inactivated fetal bovine serum (FBS, Fisher Scientific). These primary cells were then treated with 4-hydroxy-tamoxifen (1μM final, Sigma) overnight or DMSO at passage 3. For stable isotope tracing experiments, wild type (WT) MEFs were cultured for the last 24h in serum-free media (custom DMEM/F12 containing 5,5mM Glucose; 1mM Glutamine; 0,2mM Branched Chain Amino Acids and a mix

of growth factors (ATCC, #PCS201040), in presence of the MPC-1 inhibitor UK5099 (50μM, Sigma, PZ0160) for 12h and with 1mM of universally labelled ^{13}C-pyruvate (Sigma, 490717) for the last 6 hours. Skin fibroblasts isolated from Leigh syndrome patients or control individuals were cultured in DMEM complemented with 10% of heat-inactivated fetal bovine serum (FBS, Fisher Scientific). The N2A murine neuroblastoma cell line was cultured in DMEM/F12 complemented with 10% of heat-inactivated fetal bovine serum (FBS, Fisher Scientific).

RNA extraction, RNA-seq and quantitative PCR

Total RNAs were isolated from various organs or from cells using TriZol Reagent (Invitrogen). For RNA-seq, mRNA libraries were generated following the manufacturer recommendations (mRNA hyper prep from ROCHE). Bar-coded libraries were pooled and sequenced on the Novaseq6000 200 cycles ILLUMINA sequencer, with a sequencing depth corresponding to a minimum of 2x30 Millions of 100 base-pair reads per sample after demultiplexing. Quantitative real time PCR (RT-qPCR) was performed on a LightCycler 480 (Roche). cDNAs were synthesized from 500ng of total RNA using the SuperScript™ III Reverse Transcriptase (Invitrogen). The relative mRNA copy number was calculated using Ct values and was normalized to *18S* and *tubulin β5* mRNA levels. Primers used for RT-qPCR analyses are listed in the supplemental table S3. For RNA-sequencing, Star v2.5.3a was used to align reads on the reference genome mm10. Gene expression was determined with RSEM 1.2.28 on RefSeq catalogue, prior to normalisation and differential analysis with DESeq2 bioconductor package. Multiple hypothesis adjusted p-values were calculated with the Benjamini-Hochberg procedure to control FDR. Gene Set Enrichment Analysis (GSEA) was performed with fgsea bioconductor package on Hallmark gene sets from MSigDB collections, completed with some custom gene sets. For gene set enrichment analyses (GSEA), the results from the differential expression analysis performed comparing *E4f1*$^{(Nes)KO}$ and CTL embryos were used as input with the *fgsea* R package, after ranking genes according to their fold-change in expression. We

considered the Reactome database as well as the list of E4F1 known target genes for these analyses and performed 1000 permutations to define *p*-values.

Measurement of PDH activity and blood lactate levels

PDH activity was measured using Pyruvate Dehydrogenase Activity Assay Kit (MAK183-1KT, Sigma) as recommended by the manufacturer. Lactate levels were measured in blood using a lactometer (EKF Diagnostics).

Protein extraction and western blotting

Total protein extracts were prepared from isolated brains lysed in Laemmli buffer (80mM Tris pH=6,8, 2% SDS, 12% sucrose, 2% β-mercaptoethanol, bromophenol blue) and immunoblotting was performed using the following antibodies: anti- E4F1 (1/1000) (Fajas et al., 2000), C-CASP3 (Cell Signaling, 9661S, 1/1000), DLAT (Santa Cruz, sc-271534, 1/500), MPC1 (Sigma, HPA045119, 1/1000), DLD (Santa Cruz, sc-365977, 1/1000), PDHE1 (Life Technologies, 459400, 1/500), ELP3 (Abcam, ab190907, 1/500), ELP1 (Abcam, ab62498, 1/500), TUBULIN (Sigma, T6199, 1/1000) and ACTIN (Sigma, A3854, 1/7000).

LC-MS detection of tRNA modifications

Total RNAs were isolated from brains of E14.5 *E4f1*$^{(Nes)KO}$ and *CTL*$^{(Nes)}$ embryos or from MEFs using TriZol Reagent (Invitrogen). tRNAs were purified on an agarose gel. 400ng of tRNAs were digested with 0.001U of nuclease P1 (Sigma, N8630) in 25mM of ammonium acetate pH 5.3 for 2 hours at 42°C. Samples were then treated with 0.001U of alkaline phosphatase (Sigma, P4252) in 250 mM ammonium acetate pH 5.3 at 37°C for 2 hours. The nucleoside solution was diluted twice and filtered with 0.22µm filters (Millex®-GV, Millipore, SLGVR04NL). 5µL of each sample was injected in triplicate in a LC-MS/MS. For stable isotope labelling experiments using ^{13}C-sodium pyruvate (Sigma), 4ug of total RNA were digested with 0.002 U of nuclease P1 and alkaline phosphatase by following the same procedure. Nucleosides were then separated using Nexera LC-40 systems (Shimadzu) and Synergi™ Fusion-RP C18

column (4µm particle size, 250mm x 2mm, 80Å) (Phenomenex, 00G-4424-B0). Mobile phase was composed of 5mM ammonium acetate pH5.3 (solvent A) and acetonitrile (solvent B). The 30 minutes elution gradient started with 100% phase A followed by a linear gradient until reaching 8% solvent B at 13 min. Solvent B was further increased to 40% over the next 10 minutes. After 2 minutes, solvent B was decreased back to 0% at 25.5 minutes. Initial conditions were recovered by rinsing the LC-system with 100% solvent A for additional 4.5 minutes. The flow rate was set at 0.4 mL/min and the column temperature at 35 °C. Analysis was performed using a triple quadrupole 8060NX (Shimadzu corporation, Kyoto, Japan) in positive ion mode. Peak areas were measured using Skyline 21.2 software (MacCoss Lab Software; https://skyline.ms) and the ratio of modified nucleosides on non-modified nucleosides was calculated.

Quantitative chromatin immunoprecipitation (qChIP) assays

For qChIP assays in cells, N2A cells were incubated with 1% formaldehyde/1% paraformaldehyde for 5min. Nuclei were isolated and chromatin was extracted and sonicated (epishear, Active motif). qChIPs on the *Elp3* locus were carried out using a control irrelevant IgG or an affinity-purified rabbit anti-E4F1 polyclonal (Fajas et al., 2000) antibody, essentially as previously described (Rodier *et al.* Cell Reports 2015; Houles et al.). Primers used for qChIP assays are listed in the Supplemental table 3.

Lentivirus production

Lentiviral particles encoding *Flag-tagged human PDHA1* or shRNAs targeting mouse *Pdha1* (TRCN0000041914/TRCN0000041914 (Sigma)) were produced in 293T packaging cells by transient transfection using Jet-PEI reagent (Ozyme). 72h after transfection, viral supernatants were harvested and added on Mefs overnight in presence of polybrene (5µg/ml, Sigma). Selection of transduced cells was performed 48 hours after transduction with puromycin (2 µg/mL, Invitrogen).

Immunohistochemistry, Immunofluorescence and histological analyses

Embryonic brains were dissected in 0.1M phosphate-buffered saline pH7.4 (PBS) and were fixed at 4°C in 4% paraformaldehyde (PFA) for one hour. Fixed samples were cryoprotected overnight in 20% sucrose in PBS at 4°C, embedded in OCT Compound (VWR International) and sectioned (14µm) onto slides (SuperFrost Plus, VWR International) using a cryostat. Entire head samples were fixed in 4% neutral-buffered formalin (24h), decalcificated in 10% EDTA for 3 days and paraffin embedded. FFPE tissues were sectioned (4µm sections) and processed for immunohistochemistry (IHC) or hematoxylin and eosin (H/E) staining. For GFP (Invitrogen, A10262) and C-CASP3 (Cell Signaling, 9661S,) stainings, IHC was performed on a VENTANA Discovery Ultra automated staining instrument (Ventana Medical Systems) according to the manufacturer's instructions. The number of C-CASP3 positive cells were quantified on whole-slides digitized sections (Panoramic 250 Flash II/3DHISTECH whole-slide digital microscope) scanned at a 0.22 µm/pixel resolution, using Definiens Developer XD software (Definiens, Munich, Germany). IF stainings were processed manually. Briefly, brain sections were pretreated with target retrieval solution (DAKO, 20 min, 95°C) prior incubation with the following primary antibodies overnight at 4°C: anti- MCT4 (Proteintech, 22787-1-AP), ATF4 (Cell Signaling, 11815), phospho-Eif2a (Cliniscience, P04387), Ki67 (Abcam, Ab15580), SOX2 (Santa Cruz, Sc17320), TBR2 (eBiosciences, 14-4875-82), TBR1 (Abcam (Ab31940). After washing, sections were incubated for 1 hour at room temperature with either anti-rabbit, anti-rat or anti-goat secondary antibodies coupled to Alexa-488, Alexa-647 or Alexa-555 (Life Technologies). Nuclei were counterstained with DAPI (Sigma), washed in PBST and coverslipped using Mowiol mounting solution. For images analyses, sections were visualized on a Thunder epifluorescent microscope (Nikon).

High-Resolution Episcopic Microscopy (HREM)

E14.5 embryos and E16.5 heads were fixed in Bouin's fixative for 24 hours, then washed and stored in 70 % EtOH. Fixed samples were gradually dehydrated in an increasing series of ethanol concentrations and were embedded in a methacrylate resin (JB-4 kit, Polysciences,

Warrington, PA) containing eosin and acridin orange as contrasts agents as previously described (Mohun and Weninger, 2012) (https://dmdd.org.uk/hrem/). The resin blocks were sectioned on the Histo3D system to generate data by repeated removal of 7 µm thick sections (Wendling et al., 2021). Resulting HREM data with a voxel size of 8 X 8 X 7 μm^3 (E14.5 whole embryos) or 6.5 X 6.5 X 7 μm^3 (E16.5 heads) were generated from approximately 1000 or 800 aligned images, respectively. All HREM images were converted into a volume dataset and segmented using Avizo 9.4.0 software (Thermofisher Scientific, France) to create 2- and 3-dimensional (3D) images, according to the Allen brain atlas.

Statistical analysis

In vivo studies were performed on a sufficient number of animals per genotype with a minimum of 5 animals per experimental group. The in vitro data were obtained from 3 to 5 independent experiments as indicated in the figure legends. Statistical significance was evaluated using unpaired bilateral Student's *t*-test. P values inferior or equal to 0.05 were considered statistically significant.

REFERENCES

Abbassi, N.-E.-H., Biela, A., Glatt, S., Lin, T.-Y., 2020. How Elongator Acetylates tRNA Bases. IJMS 21. doi:10.3390/ijms21218209

Creppe, C., Malinouskaya, L., Volvert, M.-L., Gillard, M., Close, P., Malaise, O., Laguesse, S., Cornez, I., Rahmouni, S., Ormenese, S., Belachew, S., Malgrange, B., Chapelle, J.-P., Siebenlist, U., Moonen, G., Chariot, A., Nguyen, L., 2009. Elongator Controls the Migrationand Differentiation of Cortical Neuronsthrough Acetylation of a-Tubulin. Cell 136, 551–564.

Fajas, L., Paul, C., Vié, A., Estrach, S., Medema, R., Blanchard, J.M., Sardet, C., Vignais, M.L., 2001. Cyclin A is a mediator of p120E4F-dependent cell cycle arrest in G1. Mol. Cell. Biol. 21, 2956–2966.

Fajas, L., Paul, C., Zugasti, O., Le Cam, L., Polanowska, J., Fabbrizio, E., Medema, R., Vignais, M.L., Sardet, C., 2000. pRB binds to and modulates the transrepressing activity of the E1A-regulated transcription factor p120E4F. Proc. Natl. Acad. Sci. U.S.A. 97, 7738–7743.

Goguet-Rubio, P., Seyran, B., Gayte, L., Bernex, F., Sutter, A., Delpech, H., Linares, L.K., Riscal, R., Repond, C., Rodier, G., Kirsh, O., Touhami, J., Noel, J., Vincent, C., Pirot, N., Pavlovic, G., Herault, Y., Sitbon, M., Pellerin, L., Sardet, C., Lacroix, M., Le Cam, L., 2016. E4F1-mediated control of pyruvate dehydrogenase activity is essential for skin homeostasis. Proc Natl Acad Sci U S A. 113(39):11004-9

Hermand, D., 2020. Anticodon Wobble Uridine Modification by Elongator at the Crossroad of Cell Signaling, Differentiation, and Diseases. Epigenomes 12;4(2):7.

Hetz, C., Zhang, K., Kaufman, R.J., 2020. Mechanisms, regulation and functions of the unfolded protein response. Nat Rev Mol Cell Biol 21, 421–438.

Houlès, T., Rodier, G., Le Cam, L., Sardet, C., Kirsh, O., 2015. Genomics Data. 14;5:368-70.

Bakare AB., Lesnefsky EJ., Lyer S. 2021. Leigh Syndrome: A Tale of Two Genomes. Front Physiol 12:693734.

Jain, I.H., Zazzeron, L., Goli, R., Alexa, K., Schatzman-Bone, S., Dhillon, H., Goldberger, O., Peng, J., Shalem, O., Sanjana, N.E., Zhang, F., Goessling, W., Zapol, W.M., Mootha, V.K., 2016. Hypoxia as a therapy for mitochondrial disease. Science 352, 54–61.

Johnson, S.C., Yanos, M.E., Kayser, E.-B., Quintana, A., Sangesland, M., Castanza, A., Uhde, L., Hui, J., Wall, V.Z., Gagnidze, A., Oh, K., Wasko, B.M., Ramos, F.J., Palmiter, R.D., Rabinovitch, P.S., Morgan, P.G., Sedensky, M.M., Kaeberlein, M., 2013. mTOR inhibition alleviates mitochondrial disease in a mouse model of Leigh syndrome. Science 342, 1524–1528.

Lacroix, M., Caramel, J., Goguet-Rubio, P., Linares, L.K., Estrach, S., Hatchi, E., Rodier, G., Lledo, G., de Bettignies, C., Thépot, A., Deraison, C., Chébli, K., Hovnanian, A., Hainaut, P., Dubus, P., Sardet, C., Le Cam, L., 2010. Transcription factor E4F1 is essential for epidermal stem cell maintenance and skin homeostasis. Proc. Natl. Acad. Sci. U.S.A. 107, 21076–21081.

Lacroix, M., Rodier, G., Kirsh, O., Houlès, T., Delpech, H., Seyran, B., Gayte, L., Casas, F., Pessemesse, L., Heuillet, M., Bellvert, F., Portais, J.-C., Berthet, C., Bernex, F., Brivet, M., Boutron, A., Le Cam, L., Sardet, C., 2016. E4F1 controls a transcriptional program essential for pyruvate dehydrogenase activity. *Proc Natl Acad Sci U S A*. 113(39):10998-1003

Laguesse, S., Creppe, C., Nedialkova, D.D., Prévot, P.-P., Borgs, L., Huysseune, S., Franco, B., Duysens, G., Krusy, N., Lee, G., Thelen, N., Thiry, M., Close, P., Chariot, A., Malgrange, B., Leidel, S.A., Godin, J.D., Nguyen, L., 2015. A Dynamic Unfolded Protein Response Contributes to the Control of Cortical Neurogenesis. Developmental Cell 35, 553–567.

Le Cam, L., Lacroix, M., Ciemerych, M.A., Sardet, C., Sicinski, P., 2004. The E4F protein is required for mitotic progression during embryonic cell cycles. Mol. Cell. Biol. 24, 6467–6475.

Le Cam, L., Linares, L.K., Paul, C., Julien, E., Lacroix, M., Hatchi, E., Triboulet, R., Bossis, G., Shmueli, A., Rodriguez, M.S., Coux, O., Sardet, C., 2006. E4F1 is an atypical ubiquitin ligase that modulates p53 effector functions independently of degradation. Cell 127, 775–788.

Lee, C.F., Caudal, A., Abell, L., Gowda, G.A.N., Tian, R., 2019. Targeting NAD+ metzbolism as interventions for mitochondrial disease. Sci. Rep. 9(1):3073.

Legati, A., Reyes, A., Nasca, A., Invernizzi, F., Lamantea, E., Tiranti, V., Garavaglia, B., Lamperti, C., Ardissone, A., Moroni, I., Robinson, A., Ghezzi, D., Zeviani, M., 2016. New genes and pathomechanisms in mitochondrial disorders unraveled by NGS technologies. Biochimica et Biophysica Acta. BBA - Bioenergetics 1857(8), 1326–1335.

Lin, T.-Y., Hana Abbassi, El, N., Zakrzewski, K., Chramiec-Głąbik, A., Jemioła-Rzemińska, M., Różycki, J., Glatt, S., 2019. The Elongator subunit Elp3 is a non-canonical tRNA acetyltransferase. Nature Communications 10(1):625.

Mohun, T.J., Weninger, W.J., 2012. Embedding embryos for high-resolution episcopic microscopy (HREM). Cold Spring Harb Protoc 2012, 678–680.

Morrison, A.J., 2022. Cancer cell metabolism connects epigenetic modifications to transcriptional regulation. FEBS J 289, 1302–1314.

Morscher, R.J., Ducker, G.S., Li, S.H.-J., Mayer, J.A., Gitai, Z., Sperl, W., Rabinowitz, J.D., 2018. Mitochondrial translation requires folate-dependent tRNA methylation. Nature 554, 128–132.

Muzumdar, M.D., Tasic, B., Miyamichi, K., Li, L., Luo, L., 2007. A global double-fluorescent Cre reporter mouse. Genesis 45, 593–605.

Nitsch, S., Zorro Shahidian, L., Schneider, R., 2021. Histone acylations and chromatin dynamics: concepts, challenges, and links to metabolism. EMBO Rep 22(7), e52774.

Perry, E.A., Bennett, C.F., Luo, C., Balsa, E., Jedrychowski, M., O'Malley, K.E., Latorre-Muro, P., Ladley, R.P., Reda, K., Wright, P.M., Gygi, S.P., Myers, A.G., Puigserver, P., 2021. Tetracyclines promote survival and fitness in mitochondrial disease models. Nature Metabolism 3(1):33-42.

Petrakis, T.G., Wittschieben, B.Ã., Svejstrup, J.Q., 2004. Molecular Architecture, Structure-Function Relationship, and Importance of the Elp3 Subunit for the RNA Binding of Holo-Elongator*. J. Biol. Chem. 279, 32087–32092.

Raychaudhuri, P., Rooney, R., Nevins, J.R., 1987. Identification of an E1A-inducible cellular factor that interacts with regulatory sequences within the adenovirus E4 promoter. EMBO J. 6, 4073–4081.

Rizos, H., Diefenbach, E., Badhwar, P., Woodruff, S., Becker, T.M., Rooney, R.J., Kefford, R.F., 2003. Association of p14ARF with the p120E4F transcriptional repressor enhances cell cycle inhibition. J. Biol. Chem. 278, 4981–4989.

Rodier, G., Kirsh, O., Baraibar, M., Houlès, T., Lacroix, M., Delpech, H., Hatchi, E., Arnould, S., Severac, D., Dubois, E., Caramel, J., Julien, E., Friguet, B., Le Cam, L., Sardet, C., 2015. The Transcription Factor E4F1 Coordinates CHK1-Dependent Checkpoint and

Mitochondrial Functions. CellReports 11, 220–233.

Sun, L., Zhang, H., Gao, P., 2021. Metabolic reprogramming and epigenetic modifications on the path to cancer. Protein & Cell 1–43.

Tronche, F., Kellendonk, C., Kretz, O., Gass, P., Anlag, K., Orban, P.C., Bock, R., Klein, R., Schütz, G., 1999. Disruption of the glucocorticoid receptor gene in the nervous system results in reduced anxiety. Nat Genet 23, 99–103.

Wendling, O., Hentsch, D., Jacobs, H., Lemercier, N., Taubert, S., Pertuy, F., Vonesch, J.-L., Sorg, T., Di Michele, M., Le Cam, L., Rosahl, T., Carballo-Jane, E., Liu, M., Mu, J., Mark, M., Herault, Y., 2021. High Resolution Episcopic Microscopy for Qualitative and Quantitative Data in Phenotyping Altered Embryos and Adult Mice Using the New “Histo3D” System. Biomedicines 9(7):767.

Winkler, G.S., Kristjuhan, A., Erdjument-Bromage, H., Tempst, P., Svejstrup, J.Q., 2002. Elongator is a histone H3 and H4 acetyltransferase important for normal histone acetylation levels in vivo. Proc. Natl. Acad. Sci. U.S.A. 99, 3517–3522.

Acknowledgements

This work was supported by grants from the Agence Nationale pour la Recherche (ANR-PyrE4F), the Ligue contre le Cancer (équipe labélisée) and with the institutional support of INSERM. We are grateful for the technical support of the Montpellier Rio Imaging (MRI) and animal (RAM) facilities. Histological analyses were performed thank to the "Réseau d'Histologie Expérimentale de Montpellier" (RHEM), a facility supported by the SIRIC Montpellier Cancer (Grant INCa_Inserm_DGOS_12553), the european regional development foundation and the Occitanie region (FEDER-FSE 2014-2020 Languedoc Roussillon), REACT-EU (Recovery Assistance for Cohesion and the Territories of Europe), IBiSA and the Ligue contre le cancer. Implementation of the RNA mass spectrometry facility and the proteomic platform (PPM) are supported by the Occitanie region and the FEDER (PPRi and SMART projects). We thank members of the LLC team and Massimiliano Mazzone (VIB, Leuven) for critical reading of the manuscript. MDM, MR and CDB were supported by fellowships from the laboratory of Excellence (LABEX, "Investissements d'avenir" program, ANR-10-LABX-12-01), the SIRIC Montpellier Cancer (Grant INCa-DGOS-Inserm_12553), a grant from the Institut National contre le Cancer (INCa) and the ARC foundation. We thank Y. Herault (Institut de la clinique de la souris, Illkirch) and N. Gadot and J. Valantin (pathology department at the Centre Régional contre le Cancer de Lyon), as well as JC Portais (Restore, INSA, Toulouse) for their input in HREM, IHC and stable isotope tracing experiments. Next Generation Sequencing (NGS) was carried out on the iGenSeq core facility of the Institut du Cerveau (ICM) with the help of Y. Marie.

Author Contributions

MDM, LM, NL, and LCL designed the experiments, interpreted the data and wrote the manuscript. MDM, JTC, MH, CV, RL, TA, AF, LS, RM, LM, performed the in vivo experiments. MDM, FM, JTC, LM performed in vitro experiments. GJ and RPF performed the computational analysis of RNA-seq data. PN, BY, FPC, DP, CC, MHA, FXF, EB, LS, WO, SGT performed

the histological and HREM analyses. MDM, DBC, KBH, BF, LM, AA, DA, HC, designed and performed the MS and tracing experiments. LA, GD, RG, SC and LE provided fibroblasts from Leigh syndrome patients. All authors gave a final approval of the submitted manuscript.

Competing financial interests

The authors declare no competing financial interests

FIGURE LEGENDS

Figure 1. E4F1 plays a critical role in corticogenesis during mouse embryonic development. (A) Immunohistochemistry (IHC) analysis of GFP expression on brain sagittal sections prepared from E14.5, E16.5 and E18.5 *E4f1*$^{(Nes)KO}$ and CTL littermates. Scale bars, 2.5 mm. Images are representative of experiments performed on n=4 animals/group. (B) RT-qPCR analysis of *E4f1* mRNA levels in the indicated tissues in E18.5 *E4f1*$^{(Nes)KO}$ and CTL embryos (n≥3). (C) Quantitative immunoblot analysis of E4F1 and ACTIN (ACT) protein levels in the brain of E14.5 *E4f1*$^{(Nes)KO}$ and CTL embryos. Histobars represent the quantification of n=4 immunoblots performed on independent samples for each genotype. (D) Numbers of *E4f1*$^{(Nes)KO}$ and CTL embryos identified at different developmental stages. Expected numbers were calculated based on a normal mendelian distribution. (E-F) Analysis of brain structures in E14.5 and E16.5 *E4f1*$^{(Nes)KO}$ embryos by High Resolution Episcopic Microscopy (HREM). (E) Histobars represent the volume of the neuroepithelium tissue and of brain ventricles of *E4f1*$^{(Nes)KO}$ and CTL embryos at E14.5 and E16.5 (n≥3). (F) Representative HREM images showing the 3D volumic reconstruction of different areas of the brain (forebrain in green, midbrain in blue and hindbrain in red) and of ventricles (lateral ventricles in yellow, third ventricle in pink, mesencephalic vesicle in orange and fourth ventricle in red) of E16.5 *E4f1*$^{(Nes)KO}$ and CTL littermates (n≥4). Scale bars, 280 µm.

Data are presented as mean + standard error of the mean (SEM) for Fig. 1B or standard deviation (SD) for Fig. 1C and 1E from the indicated number of animals. Statistical significance was evaluated using unpaired bilateral Student's *t*-test (ns, not significant).

See also Supplemental Figure S1.

Figure 2. *E4f1* inactivation impairs neuronal development during mid-corticogenesis. (A) Left panels: immunoblot analysis of uncleaved and cleaved CASPASE 3 (CASP3 and C-CASP3, respectively) and ACTIN (ACT, loading control) protein levels in the brain of E14.5, E16.5 and E18.5 *E4f1*$^{(Nes)KO}$ and CTL embryos. Right panel: Histobars represent the

quantification of immunoblot analyses of the ratio C-CASP3/CASP3 protein levels in the brain of *E4f1*$^{(Nes)KO}$ and CTL embryos at the indicated developmental stage (n=4 animals/group). (B) IHC analysis of C-CASP3 in brain sagittal sections prepared from E14.5, E16.5 and E18.5 *E4f1*$^{(Nes)KO}$ and CTL embryos. Insets show images at higher magnification of the forebrain neuroepithelium. Images are representative of experiments performed on n=4 to 7 animals/group. Scale bars, 100 µm and 20 µm for the insets. Red arrows point the C-CASP3 positive cells. Fb= forebrain; LV= lateral ventricule. (C) Histobars represent the number of C-CASP3 positive cells in different brain regions of *E4f1*$^{(Nes)KO}$ and CTL embryos (n≥4 animals/group). (D) Immunofluorescence (IF) analysis of SOX2, TBR2, TBR1, C-CASP3 and Ki67 protein levels in brain coronal sections prepared from E14.5 *E4f1*$^{(Nes)KO}$ and CTL embryos. Scale bars, 50 µm. Histobars represent the number of positive cells for the indicated protein marker expressed as % of the control (n≥3).

Data are presented as mean + standard deviation (SD) for Fig. 2A or standard error of mean (SEM) for Fig. 2C and 2D from the indicated animals. Statistical significance was evaluated using unpaired bilateral Student's *t*-test (ns, not significant).

See also Supplemental Fig. S2

Figure 3. Gene expression profile of E4F1-deficient neurons. (A-B) RNA-seq analysis of brains prepared from E14.5, *E4f1*$^{(Nes)KO}$ and CTL embryos (n=3 for each genotype). (A) Heatmap representing the relative mRNA levels (fold change, $\log_2$ ratio) of the differentially expressed genes (DEG) with the most statistically significant False Discovery Rate (FDR-adjusted p value). (B) Volcano plot depicting the significance (FDR) and magnitude of difference (fold change, $\log_2$ ratio) of DEG identified in E14.5 *E4f1*$^{(Nes)KO}$ embryos. (C) Gene set enrichment analysis (GSEA) of RNA-seq data showing decreased expression of E4F1 target genes. The normalized enrichment score (NES) and false discovery rate (FDR) are indicated. (D) The mRNA levels of *E4f1* and a subset of its direct target genes (*Ndufs5*, *Dnajc19*, *Taz*, *Wdr7*, *Neurl4*) were determined by RT-qPCR analysis in total RNAs prepared

from the forebrain of E14.5 *E4f1*$^{(Nes)KO}$ and CTL embryos (n=5). Data are presented as mean + standard error of the mean (SEM) for the indicated number of animals. Statistical significance was evaluated using unpaired bilateral Student's *t*-test. (E) List of the top 10 pathways identified by GSEA as differentially modulated in E14.5 *E4f1*$^{(Nes)KO}$ embryos. The size of the histobars represents the number of genes in the indicated category with an adjusted p value ≤ 0,001. (F) GSEA showing the induction of the Unfolded Protein Response (UPR) stress signature in E14.5 *E4f1*$^{(Nes)KO}$ embryos.

See also Supplemental Fig. S3 and supplemental tables S1 and S2.

Figure 4. E4F1 regulates pyruvate metabolism in neurons. (A) RT-qPCR analysis of *E4f1* mRNA levels and those of genes encoding key subunits or regulators of the pyruvate dehydrogenase complex (PDC) (*Dlat*, *Dld*, *Mpc1*, *Pdpr*, and *Pdha1*) in the forebrain of E14.5 *E4f1*$^{(Nes)KO}$ and CTL embryos (n=5 animals/group). (B) Immunoblot analysis of E4F1, DLAT, MPC1, DLD, PDHA1, and ACTIN (loading control) protein levels in the brain of E14.5 *E4f1*$^{(Nes)KO}$ and CTL embryos. Right panel: Histobars represent the quantification of immunoblots performed on n=4 independent samples/group. (C) PDH activity in protein extracts prepared from E18.5 *E4f1*$^{(Nes)KO}$ and CTL embryos (n=5 animals/group). (D) Blood lactate levels in E18.5 *E4f1*$^{(Nes)KO}$ and CTL embryos (n≥40 animals/group). (E) IF analysis of MCT4 protein levels in brain sagittal sections prepared from E14.5 *E4f1*$^{(Nes)KO}$ and CTL embryos. Fb= forebrain; Mb= middle brain; LV= lateral ventricule. Scale bars, 50 µm.

Data are presented as mean + standard error of mean (SEM) for Fig. 4A and 4C or mean + standard deviation (SD) for Fig. 4B and 4D from the indicated number of animals. Statistical significance was evaluated using unpaired bilateral Student's *t*-test (ns, not significant).

Figure 5. E4F1 controls the Elongator complex and tRNAs editing in neurons. (A) E4F1 ChIP-Seq read densities in transformed MEFs (tMEFs) and mouse ES cells (mES) at the *Elp3* locus. The sequence and the position of the E4F1 consensus motif in the *Elp3* locus are indicated. Arrows indicate gene orientation. (B) Quantitative ChIP (qChIP) experiments on the

Elp3 promoter region using an anti-E4F1 polyclonal antibody (E4F1) or an irrelevant antibody (irr) and chromatin prepared from neuronal N2A cells (n= 3 independent experiments). Results are represented as the relative ratio between the mean value of immunoprecipitated chromatin (calculated as a percentage of the input) with the anti-E4F1 antibody and the one obtained with the control antibody. (C) RT-qPCR analysis of *Elp1*, *Elp2*, *Elp3*, and *Elp4* mRNA levels in total RNAs prepared from the brain of E14.5 *E4f1*$^{(Nes)KO}$ and CTL embryos (n=5 animals/group). (D) Immunoblot analysis showing ELP1, ELP3 and ACTIN (ACT, loading control) protein levels in the brain of E14.5 *E4f1*$^{(Nes)KO}$ and CTL embryos. Right panel: Histobars represent the quantification of immunoblots performed on n≥4 independent samples. (E) Liquid-chromatography coupled to tandem mass spectrometry (LC-MS/MS) analysis of the 5-carbamoylmethyl uridine (ncm^5 U_{34}), 5-methoxy-carbonyl-methyl-2-thio uridine (mcm^{5}s^2 U_{34}) tRNAs modifications. The abundance of methyl-3-cytosine (m3C) and methylguanosine (Gm) that are unrelated to the Elongator complex were used as controls. The relative abundance of these tRNAs modifications was normalized to the total amount of Uridine (U), Cytosine (C) or Guanosine (G) (n=5 independent samples/group). (F) IHC analysis of ATF4 protein levels in brain sagittal sections prepared from E14.5 *E4f1*$^{(Nes)KO}$ and CTL embryos. Data are representative of n=4 independent experiments. Scale bars, 100 µm. (G) IF analysis of phospho-EiF2a (P-EiF2a) protein levels in brain sagittal sections prepared from E14.5 *E4f1*$^{(Nes)KO}$ and CTL embryos. Data are representative of n=4 independent experiments. Scale bars, 50 µm. (H) Histobars represent the relative mRNA levels of genes related to the ISR response in the forebrain of E14.5 *E4f1*$^{(Nes)KO}$ and CTL embryos determined by RT-qPCR (n=5 independent samples/group).

Data are presented as mean + standard error of the mean (SEM) from the indicated number of samples. Statistical significance was evaluated using unpaired bilateral Student's *t*-test (ns, not significant). Fb, forebrain; LV, lateral ventricule; Mb, midbrain.

See also Supplemental Fig. S4.

Figure 6. E4F1 coordinates AcCoA production by the PDC and its utilization by the Elongator complex to ensure U_{34} tRNAs editing. (A) RT-qPCR analysis of *E4f1*, *Dlat* and *Elp3* mRNA levels in *E4f1*^{KO} and CTL MEFs (n=4 independent populations of MEFs / group). Cells were harvested 5 days after Cre-mediated inactivation of *E4f1*. (B) Left panel: Immunoblot analysis of E4F1, DLAT, ELP3 and TUBULIN (TUB, loading control) protein levels in the same cells than in (A). Right panel: Histobars represent the quantification of immunoblots performed on independent samples (n=4 populations/group). (C) LC-MS/MS analysis of ncm^5U_{34}, $mcm^5s^2U_{34}$ and Um (internal control) in tRNAs purified from the same cells than in (A). The relative abundance of these tRNAs modifications was normalized to the total amount of Uridine (U) (n=4 independent populations of MEFs/group). (D) Schematic representation of the contribution of pyruvate to U_{34} tRNAs modifications by the Elongator complex when cells are incubated with uniformly labelled [U-^{13}C]-pyruvate. (E) Stable isotope tracing experiments in MEFs incubated for 16 hours with DMSO or the MPC1 inhibitor UK-5099 (50 uM) and cultured for the last 6 hours in the presence of [U-^{13}C]-pyruvate. ^{13}C-enrichment in ncm^5U_{34} and $mcm^5s^2U_{34}$ was determined by LC-MS/MS in two independent experiments performed in triplicates. Data are represented as the relative ratio between the ^{13}C-labelled m+2 isotopologue and the corresponding unlabelled U_{34} modification. (F) Immunoblot analysis of PDHA1, ELP3 and TUB (loading control) protein levels in MEFs transduced with lentiviruses encoding a control of *Pdha1* shRNAs (sh*Pdha1* #1 and #2). Right panel: Histobars represent the quantification of immunoblots performed on n=4 independent samples. (G) Immunoblot analysis of ELP3 and ACTIN (ACT, loading control) protein levels in human skin fibroblasts isolated from Leigh syndrome patients harboring mutations in the indicated genes or from age-matched healthy donors. (H) Immunoblot analysis of PDHA1, ELP3 and ACT (loading control) protein levels in human skin fibroblasts isolated from Leigh syndrome patients harboring mutations in the *PDHA1* gene upon transduction with an empty control or a WT-PDHA1 encoding retrovirus. Right panel: Histobars represent the quantification of immunoblots performed on cells isolated from n=3 Leigh syndrome patients.

Data are presented as mean + standard error of the mean (SEM) for Fig. 6A and 6C or standard deviation (SD) for Fig. 6B, 6E, 6F and 6H from the indicated number of samples. Statistical significance was evaluated using unpaired bilateral Student's *t*-test (ns, not significant).

SUPPLEMENTAL INFORMATION

Supplemental Figure 1. E4F1 deficiency in the CNS results in microcephaly. (A) Schematic representation of the crosses used to generate mice lacking E4F1 in the central nervous system (CNS). (B) Immunohistochemistry (IHC) analysis of GFP on whole embryo sagittal sections prepared from E14.5 *E4f1*$^{(Nes)KO}$ and CTL littermates. Scale bars, 2.5 mm. Data are representative of experiments performed on n=3 animals/group. (C) Microphotograph of E18.5 *E4f1*$^{(Nes)KO}$ and CTL littermates. Scale bars, 500 µm. (D) Weight of *E4f1*$^{(Nes)KO}$ and CTL embryos at the indicated embryonic developmental stages. N indicates the number of embryos analyzed for each group. (E) Left panel: microphotograph of cortex isolated from E18.5 embryos *E4f1*$^{(Nes)KO}$ and CTL embryos. Right panel: Histobars represent the width and the length of the cortex these embryos (n=4 animals/group). Data were normalized according to each embryo total body length. Data are presented as mean + standard deviation (SD) from the indicated number of animals. Statistical significance was evaluated using unpaired bilateral Student's *t*-test (ns, not significant).

Supplemental Figure 2. (A) Analysis of brain lesions in E14.5 and E16.5 *E4f1*$^{(Nes)KO}$ and CTL embryos by High Resolution Episcopic Microscopy (HREM). Histobars represent the volume of different regions of the neuroepithelium tissue and of brain ventricles of E14.5 and E16.5 *E4f1*$^{(Nes)KO}$ and CTL embryos (n≥3). Data are presented as mean + standard deviation (SD) from the indicated number of animals. Statistical significance was evaluated using unpaired bilateral Student's *t*-test. (B) Representative HREM images showing the 3D volumic reconstruction of different areas of the brain neural tissue (forebrain in green, midbrain in blue, and hindbrain in red) and of the ventricular system (lateral ventricles in yellow, third ventricle in pink, mesencephalic vesicle in orange, fourth ventricle in red) of E14.5 *E4f1*$^{(Nes)KO}$ and CTL littermates. Scale bars, 175 µm. (C) Hematoxylin and eosin (H&E) -stained sagittal sections prepared from E14.5 and E16.5 *E4f1*$^{(Nes)KO}$ and CTL embryos. The red and green insets show images at higher magnification of the forebrain and hindbrain of the same embryos. Scale bars,

2.5 mm and 100 µm for the insets. (D) Schematic representation of embryonic neurogenesis. The different protein markers used to distinguish apical and intermediate progenitors and neurons are indicated. (E) Schematic representation of the dorso-lateral region of the medial plane used to determine the relative numbers of the different neuronal progenitors and their respective proliferation cell survival rates by immunofluorescence.

Supplemental Figure 3. (A) RNA-seq analysis of total brain prepared from E14.5 *E4f1*$^{(Nes)KO}$ and CTL embryos. The list indicates the relative mRNA levels (fold change, log2) of the top 20 differentially expressed genes (DEG) with the most statistically significant False Discovery Rate (FDR-adjusted p value) identified in E14.5 *E4f1*$^{(Nes)KO}$ embryos. Genes indicated in green and purple are E4F1-direct target genes and UPR-related genes, respectively. (B) Venn diagram showing the overlap between DEG identified in E14.5 *E4f1*$^{(Nes)KO}$ embryos by RNA-seq and the list of E4F1-direct target genes identified in tMEFs, MEFs, and ES cells by ChIP-seq analyses and gene expression profiling (RNA-seq and microarrays). (C) *E4f1* mRNA levels and those of a subset of E4F1 direct target genes (*Ndufs5*, *Dnajc19*, *Dlat*, *Mpc1*, *Pdpr*, and *Dld*), or of *Pdha1* (used as a control) were determined by RT-qPCR analysis using total RNAs prepared from total brain of E14.5 *E4f1*$^{(Nes)KO}$ and CTL embryos (n=5). Data are presented as mean + standard deviation (SD) from the indicated number of animals. Statistical significance was evaluated using unpaired bilateral Student's *t*-test. (D) Gene set enrichment analysis (GSEA) of DEG identified in E14.5 *E4f1*$^{(Nes)KO}$ embryos. The size of the histobars represent the number of genes in each category and the color correspond to the indicated adjusted p value.

Supplemental Figure 4. (A) RT-qPCR analysis of Elongator complex subunit *Elp1*, *Elp2*, *Elp3*, *Elp4* mRNA levels in total brains of E14.5, E16.5, E18.5 *E4f1*$^{(Nes)KO}$ and CTL embryos (n=5 animals/group). (B) Schematic representation of the cascade leading to U_{34} tRNAs modifications. The enzymes catalyzing the different steps are indicated in bold. (C) RT-qPCR analysis of Gln, Glu and Lys tRNA levels in E14.5, *E4f1*$^{(Nes)KO}$ and CTL embryos (n=5 animals/group). (D) Immunoblot analysis of acetylated α–tubulin (α–TUBac), total α–tubulin

(α–TUB), acetylated lysine 14 of histone H3 (H3K14ac), total histone H3 (H3) and ACTIN (ACT, loading control) protein levels in E14.5 *E4f1*$^{(Nes)KO}$ and CTL embryos. Lower panel: histobars represent the quantification of immunoblots performed on n≥3 independent samples. (E) Schematic representation of the different transitions and their respective molecular weight of the m+2 isotopologues of the indicated U_{34} tRNA modifications detected by LC-MS/MS upon incubation with [U-^{13}C]-pyruvate.

Data are presented as mean + standard error of the mean (SEM) for Fig. S4A and S4C or mean + standard deviation (SD) for Fig. S4D from the indicated number of animals. Statistical significance was evaluated using unpaired bilateral Student's *t*-test (ns, not significant).

Supplemental Table S1

RNA-seq analysis of differentially expressed genes (DEG) in the brain of E14.5 *E4f1*$^{(Nes)KO}$ embryos.

Supplemental Table S2

List of genes defining E4F1 core targets. This list was defined by selecting genes harboring an E4F1 ChIP-seq peak in tMEFs or mES cells, and showing differential expression between *E4f1*^{KO} vs CTL tMEFs, *E4f1*^{KO} vs CTL MEFs, and between *E4f1*$^{(Nes)KO}$ and CTL neurons.

Supplemental Table S3

List of oligonucleotides used in this study.

Figure 1

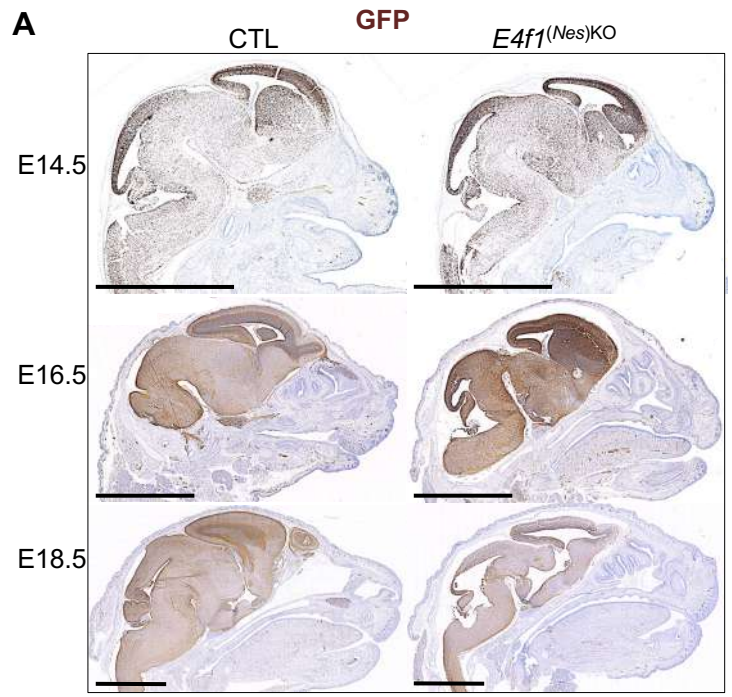

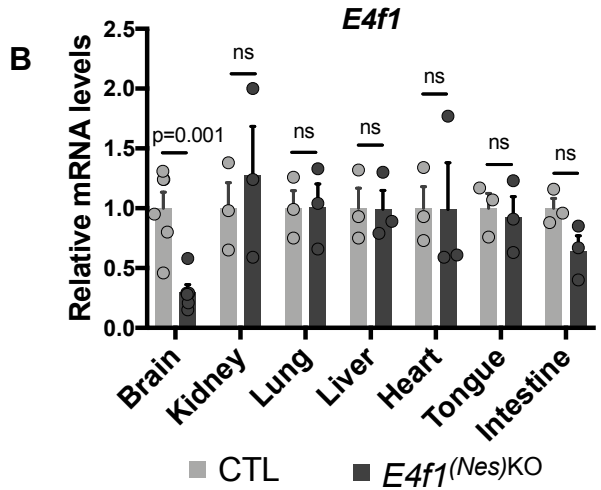

D

Number of mouse embryos

		Expected (%)	Observed (%)
E14.5	CTL	205 (75)	182 (67)
	E4f1 $^{(Nes)}$KO	68 (25)	91 (33)
E16.5	CTL	159 (75)	151 (71)
	E4f1 $^{(Nes)}$KO	53 (25)	61 (29)
E18.5	CTL	166 (75)	153 (69)
	E4f1 $^{(Nes)}$KO	55 (25)	68 (31)
P1	CTL	54 (75)	72 (100)
	E4f1 $^{(Nes)}$KO	18 (25)	0 (0)

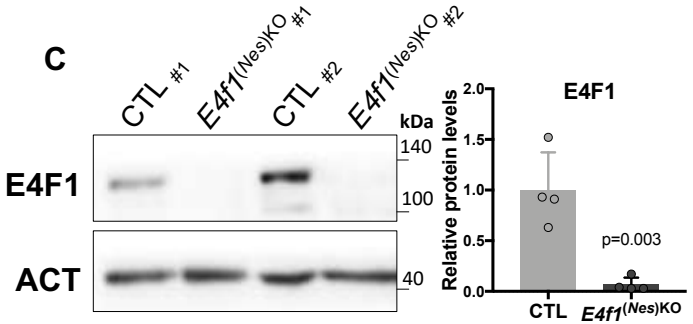

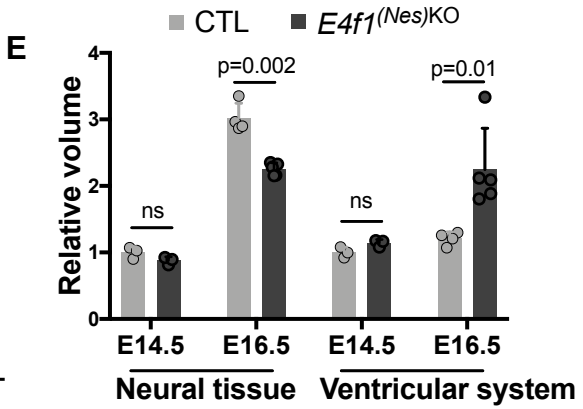

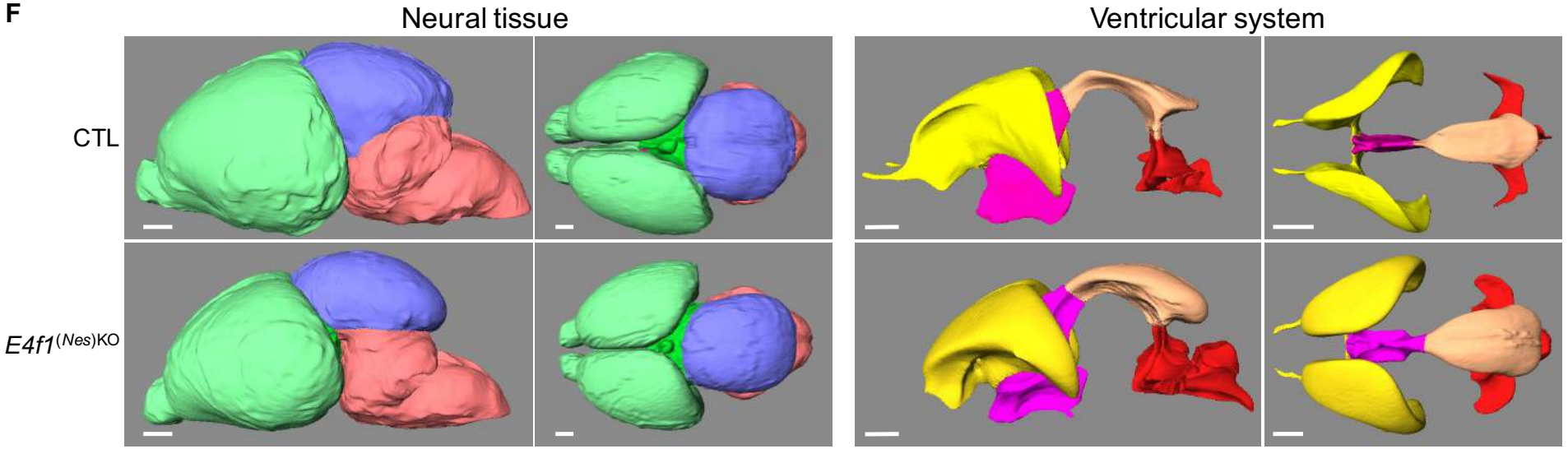

Figure 2

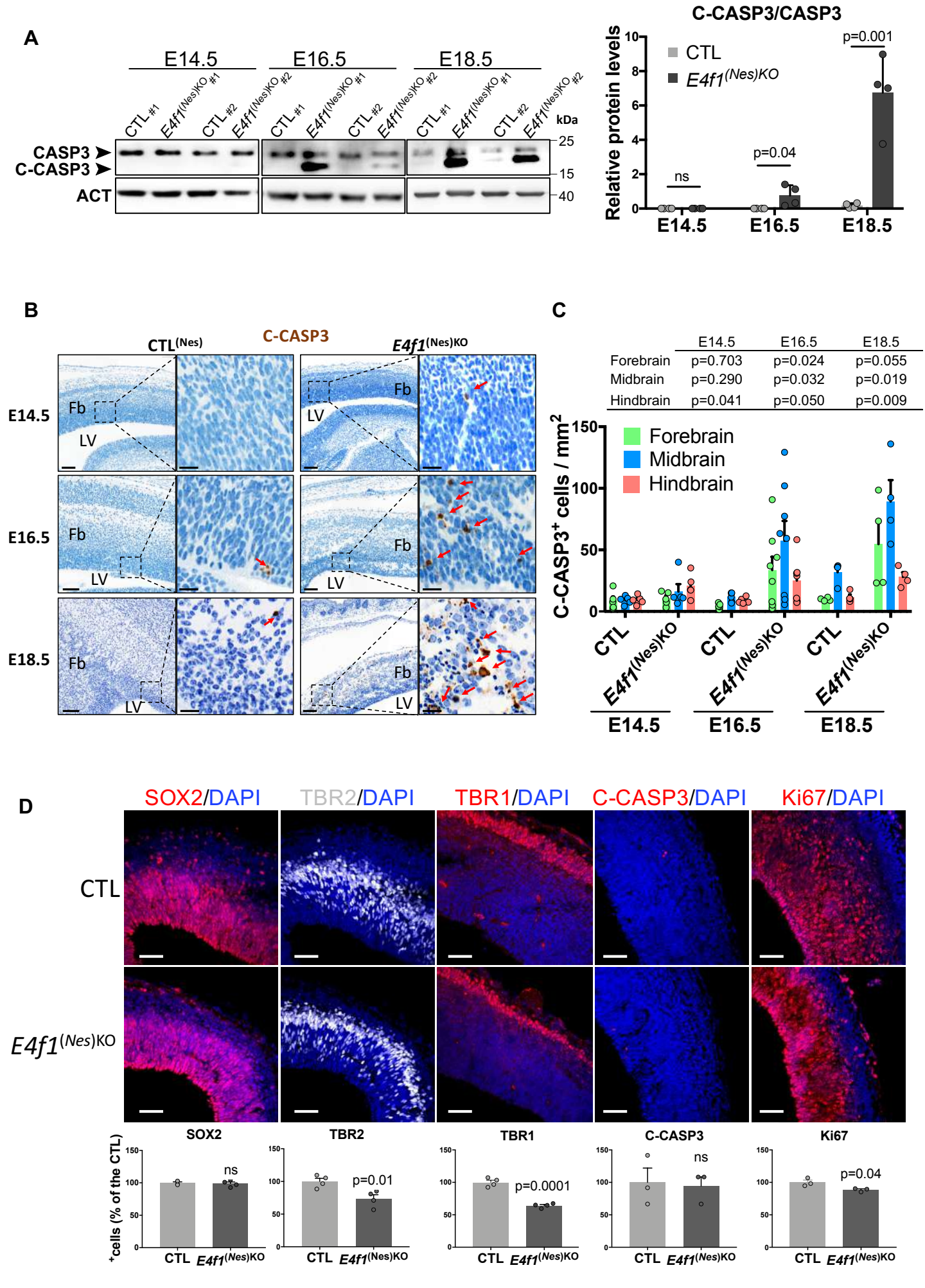

	E14.5	E16.5	E18.5
Forebrain	p=0.703	p=0.024	p=0.055
Midbrain	p=0.290	p=0.032	p=0.019
Hindbrain	p=0.041	p=0.050	p=0.009

Figure 3

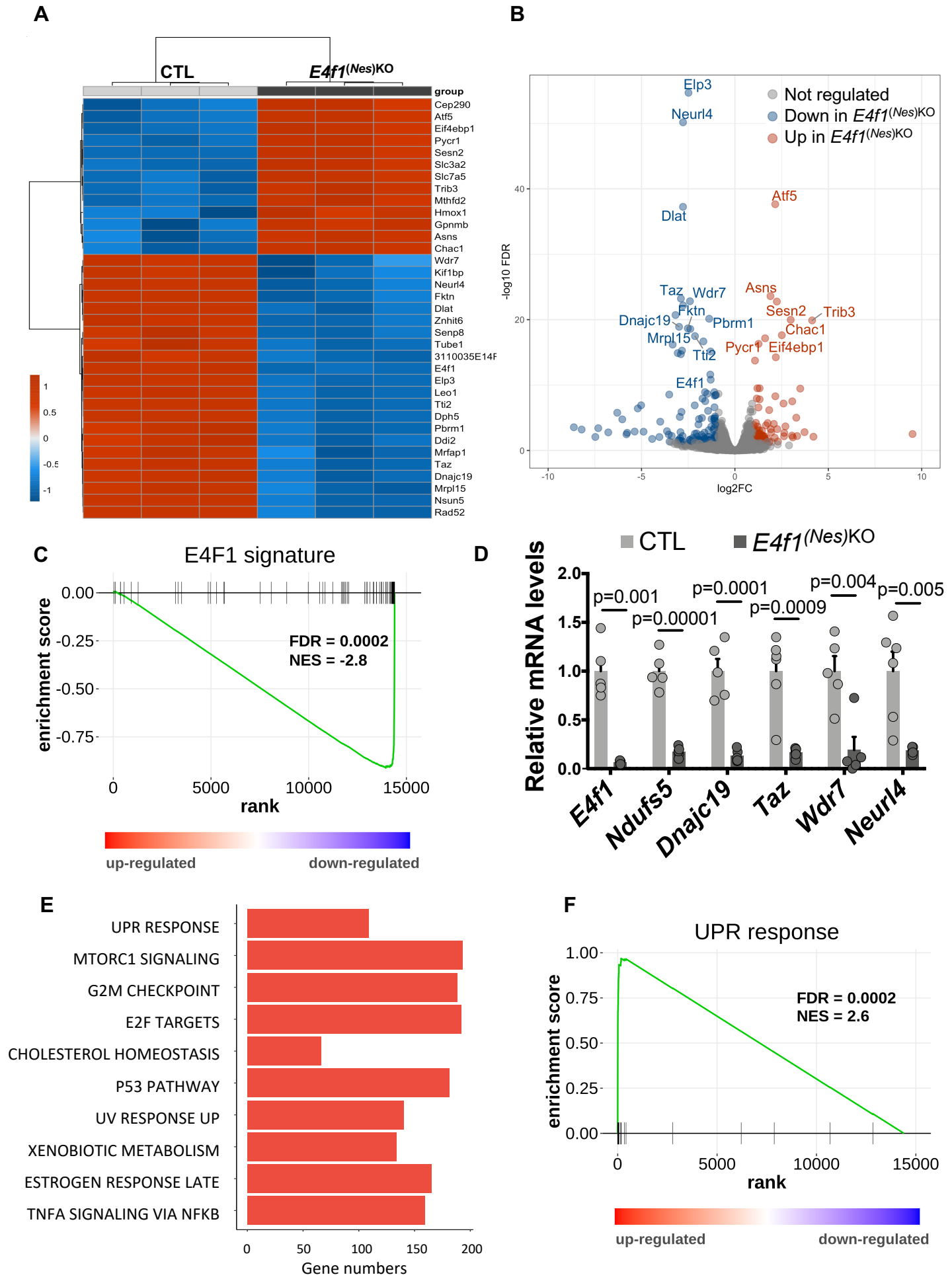
A
CTL
E4f1(Nes)KO
group
Cep290
Atf5
Eif4ebp1
Pycr1
Sesn2
Slc3a2
Slc7a5
Trib3
Mthfd2
Hmox1
Gpnmb
Asns
Chac1
Wdr7
Kif1bp
Neurl4
Fktn
Dlat
Znhit6
Senp8
Tube1
3110035E14F
E4f1
Elp3
Leo1
Tti2
Dph5
Pbrm1
Ddi2
Mrfap1
Taz
Dnajc19
Mrpl15
Nsun5
Rad52
B
Not regulated
Down in E4f1(Nes)KO
Up in E4f1(Nes)KO
-log10 FDR
log2FC
C
E4F1 signature
enrichment score
FDR = 0.0002
NES = -2.8
rank
up-regulated
down-regulated
D
CTL
E4f1(Nes)KO
Relative mRNA levels
p=0.001
p=0.00001
p=0.0001
p=0.0009
p=0.004
p=0.005
E4f1
Ndufs5
Dnajc19
Taz
Wdr7
Neurl4
E
UPR RESPONSE
MTORC1 SIGNALING
G2M CHECKPOINT
E2F TARGETS
CHOLESTEROL HOMEOSTASIS
P53 PATHWAY
UV RESPONSE UP
XENOBIOTIC METABOLISM
ESTROGEN RESPONSE LATE
TNFA SIGNALING VIA NFKB
Gene numbers
F
UPR response
enrichment score
FDR = 0.0002
NES = 2.6
rank
up-regulated
down-regulated

Figure 4

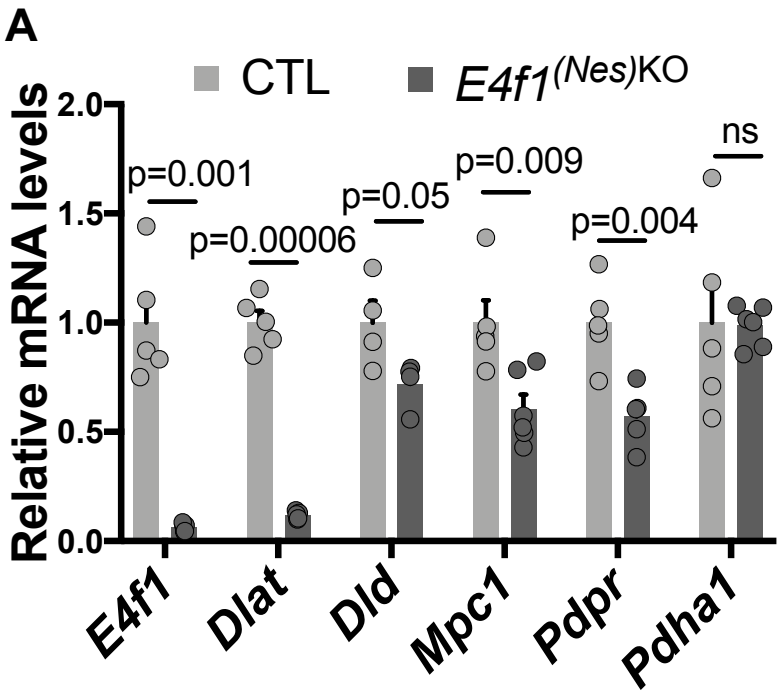
A
CTL
E4f1(Nes)KO
Relative mRNA levels
2.0
1.5
1.0
0.5
0.0
p=0.001
p=0.00006
p=0.05
p=0.009
p=0.004
ns
E4f1
Dlat
Dld
Mpc1
Pdpr
Pdha1

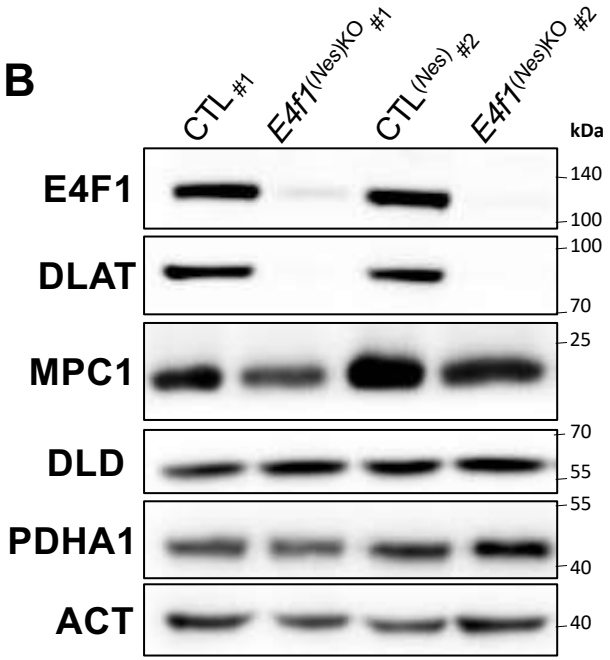
B
CTL #1
E4f1(Nes)KO #1
CTL(Nes) #2
E4f1(Nes)KO #2
kDa
E4F1
DLAT
MPC1
DLD
PDHA1
ACT
140
100
100
70
25
70
55
55
40
40

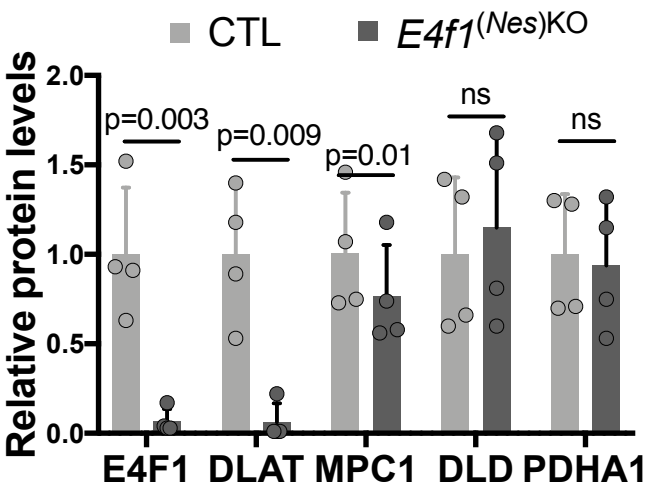
CTL
E4f1(Nes)KO
Relative protein levels
2.0
1.5
1.0
0.5
0.0
p=0.003
p=0.009
p=0.01
ns
ns
E4F1
DLAT
MPC1
DLD
PDHA1

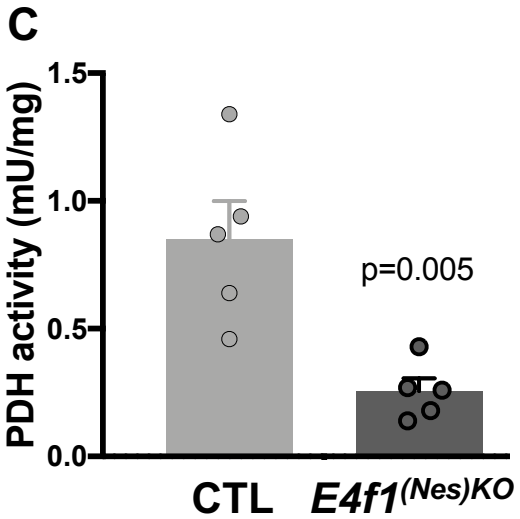
C
PDH activity (mU/mg)
1.5
1.0
0.5
0.0
p=0.005
CTL
E4f1(Nes)KO

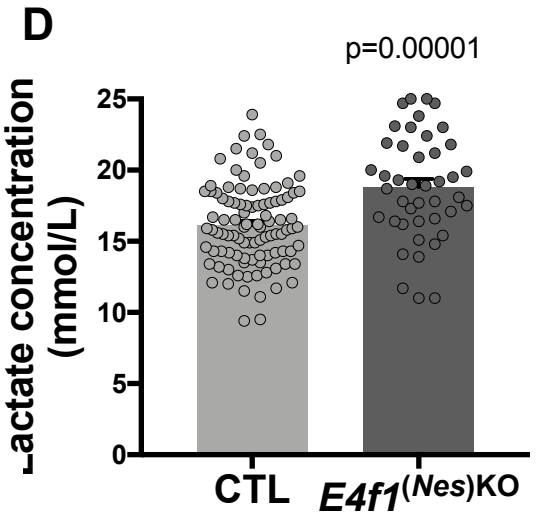
D
p=0.00001
Lactate concentration (mmol/L)
25
20
15
10
5
0
CTL
E4f1(Nes)KO

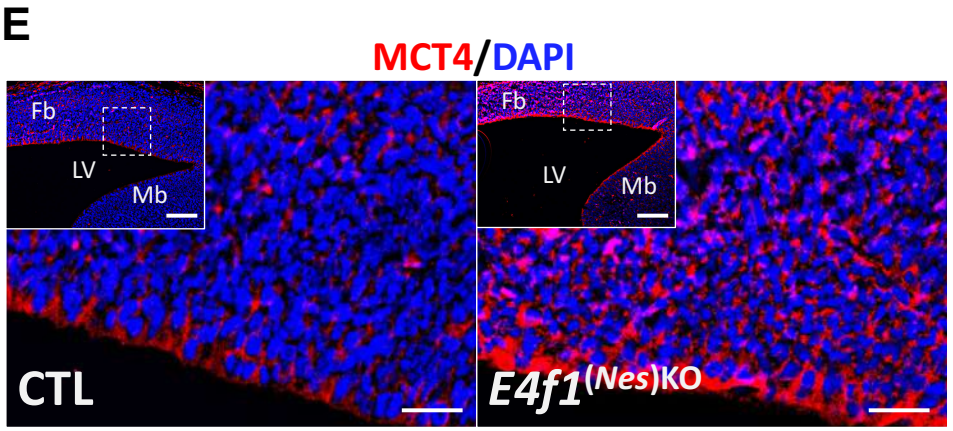
E
MCT4/DAPI
Fb
LV
Mb
Fb
LV
Mb
CTL
E4f1(Nes)KO

Figure 5

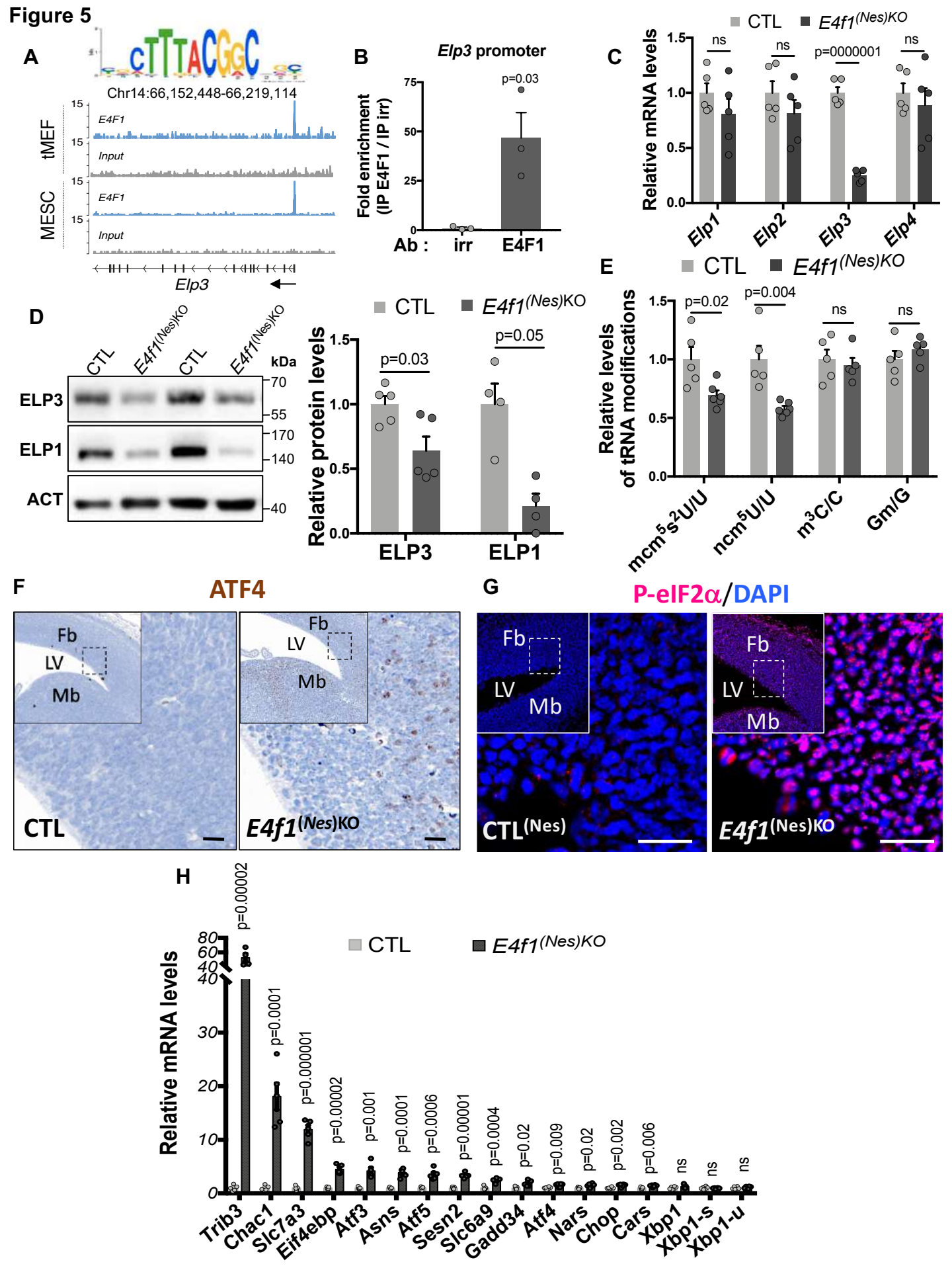
A
Chr14:66,152,448-66,219,114
tMEF
MESC
E4F1
Input
Elp3
B
Elp3 promoter
Fold enrichment (IP E4F1 / IP irr)
p=0.03
Ab : irr E4F1
C
CTL
E4f1(Nes)KO
Relative mRNA levels
ns
p=0000001
Elp1
Elp2
Elp3
Elp4
D
CTL
E4f1(Nes)KO
kDa
ELP3
ELP1
ACT
Relative protein levels
p=0.03
p=0.05
E
Relative levels of tRNA modifications
p=0.02
p=0.004
mcm5s2U/U
ncm5U/U
m3C/C
Gm/G
F
ATF4
Fb
LV
Mb
CTL
E4f1(Nes)KO
G
P-eIF2α/DAPI
CTL(Nes)
E4f1(Nes)KO
H
Relative mRNA levels
p=0.00002
p=0.0001
p=0.000001
p=0.00002
p=0.001
p=0.0001
p=0.0006
p=0.00001
p=0.0004
p=0.02
p=0.009
p=0.02
p=0.002
p=0.006
ns
Trib3
Chac1
Slc7a3
Eif4ebp
Atf3
Asns
Atf5
Sesn2
Slc6a9
Gadd34
Atf4
Nars
Chop
Cars
Xbp1
Xbp1-s
Xbp1-u

Figure 6

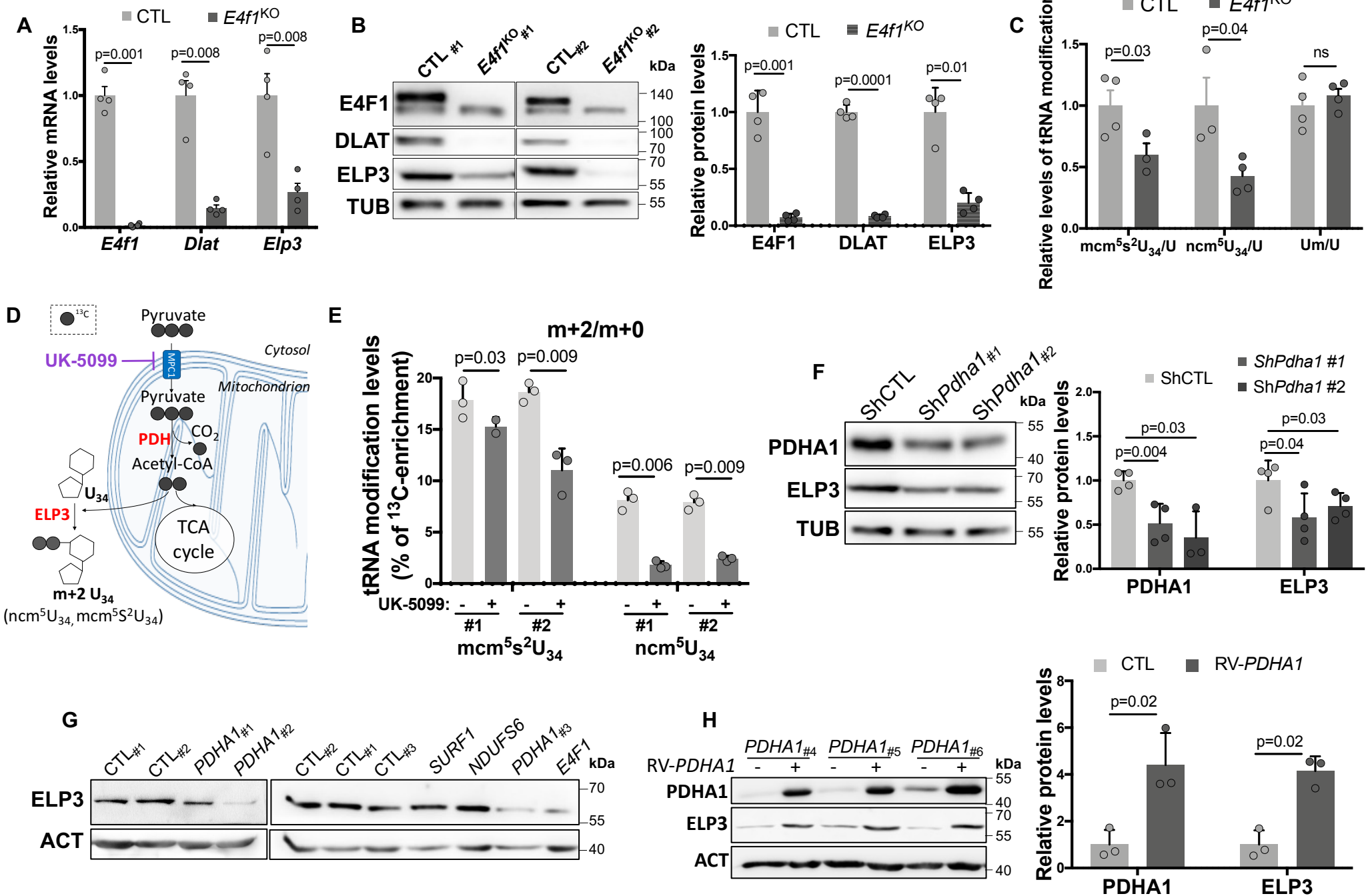
A
CTL
E4f1KO
Relative mRNA levels
p=0.001
p=0.008
p=0.008
E4f1
Dlat
Elp3
B
CTL #1
E4f1KO #1
CTL#2
E4f1KO #2
kDa
E4F1
DLAT
ELP3
TUB
140
100
100
70
70
55
55
Relative protein levels
p=0.001
p=0.0001
p=0.01
E4F1
DLAT
ELP3
C
Relative levels of tRNA modifications
p=0.03
p=0.04
ns
mcm5s2U34/U
ncm5U34/U
Um/U
D
13C
Pyruvate
UK-5099
MPC1
Cytosol
Mitochondrion
Pyruvate
PDH
CO2
Acetyl-CoA
U34
ELP3
TCA cycle
m+2 U34
(ncm5U34, mcm5S2U34)
E
m+2/m+0
tRNA modification levels
(% of 13C-enrichment)
p=0.03
p=0.009
p=0.006
p=0.009
UK-5099: - + - + - + - +
#1
#2
#1
#2
mcm5s2U34
ncm5U34
F
ShCTL
ShPdha1 #1
ShPdha1 #2
kDa
PDHA1
ELP3
TUB
55
40
70
55
55
Relative protein levels
p=0.03
p=0.004
p=0.03
p=0.04
PDHA1
ELP3
G
CTL#1
CTL#2
PDHA1#1
PDHA1#2
CTL#2
CTL#1
CTL#3
SURF1
NDUFS6
PDHA1#3
E4F1
kDa
ELP3
ACT
70
55
40
H
PDHA1#4
PDHA1#5
PDHA1#6
RV-PDHA1
- + - + - +
kDa
PDHA1
ELP3
ACT
55
40
70
55
40
CTL
RV-PDHA1
Relative protein levels
p=0.02
p=0.02
PDHA1
ELP3